INL/RPT-22-70388-Rev000

Demonstrate Improved Ag Diffusion and Describe the Basis for Pd Penetration Modeling in SiC

September 30, 2022

Technical Report

Larry K. Aagesen[1], Chao Jiang[1], Wen Jiang[1], Jia-Hong Ke[1],
Pierre-Clément A. Simon[1], and Lin Yang[1,2]

[1]Idaho National Laboratory
[2]University of Florida

Idaho National Laboratory

*INL is a U.S. Department of Energy National Laboratory
operated by Batelle Energy Alliance, LLC*

Demonstrate Improved Ag Diffusion and Describe the Basis for Pd Penetration Modeling in SiC

Technical Report

Larry K. Aagesen[1], Chao Jiang[1], Wen Jiang[1], Jia-Hong Ke[1], Pierre-Clément A. Simon[1], and Lin Yang[1,2]

[1]Idaho National Laboratory
[2]University of Florida

September 30, 2022

Idaho National Laboratory
Computational Mechanics and Materials Department
Idaho Falls, Idaho 83415

http://www.inl.gov

Prepared for the
U.S. Department of Energy
Office of Nuclear Energy
Under U.S. Department of Energy-Idaho Operations Office
Contract DE-AC07-05ID14517

Page intentionally left blank

Abstract

In past work, an effective diffusivity coefficient was determined for Ag transport through the silicon carbide layer of a tristructural isotropic fuel particle. The effective diffusivity coefficient accounts for the microstructure of the silicon carbide and includes both bulk diffusion and grain boundary diffusion of Ag. In this report, the model has been improved by accounting for the enhanced concentration of vacancies in the bulk due to irradiation, which substantially influence bulk diffusivity at low temperatures. To improve the BISON model and make it fission rate dependent, effective diffusivity calculations have been performed that incorporate the radiation-modified bulk diffusivity. The microstructure and irradiation-dependent effective diffusivity has also been implemented into BISON, and its predictions for Ag release from tristructural isotropic fuel have been successfully compared to AGR-1 post-irradiation measurements. Moreover, a new feature has been developed in the Multiphysics Object-Oriented Simulation Environment (MOOSE) to account for different grain boundary types. The Ag diffusivity in Σ5 (210)/[001] grain boundaries has been computed and was found to be greater than in random high-angle grain boundaries. The presence of the fission product Pd can also have an important effect on the properties of the silicon carbide layer in tristructural isotropic particles. The penetration of Pd into the silicon carbide layer causes a corrosion reaction that can lead to the failure of the silicon carbide layer; however, this corrosion reaction is not well understood. To enable an improved understanding of the mechanism, ab-initio molecular dynamics simulations of Pd interaction with bulk silicon carbide have been performed. The improved understanding of the reaction will form a basis for future improvements to the BISON's Pd penetration failure model.

Acknowledgments

This report was authored by a contractor of the U.S. Government under contract DE-AC07-05ID14517. Accordingly, the U.S. Government retains a non-exclusive, royalty-free license to publish or reproduce the published form of this report, or allow others to do so, for U.S. Government purposes. Funding was provided by the Nuclear Energy Advanced Modeling and Simulation (NEAMS) program.

This research made use of the resources of the High Performance Computing Center at Idaho National Laboratory, which is supported by the DOE Office of Nuclear Energy and the Nuclear Science User Facilities under contract no. DE-AC07-05ID14517.

Page intentionally left blank

Contents

List of Figures

List of Tables

1. INTRODUCTION

Several next-generation nuclear reactor designs currently under consideration use tristructural isotropic (TRISO) fuel particles. A TRISO particle has a fuel kernel at its center, which is coated with a porous carbon buffer layer, an inner pyrolytic carbon (IPyC) layer, a silicon carbide (SiC) layer, and an outer pyrolytic carbon (OPyC) layer [1]. The SiC layer is the primary barrier that prevents the release of most fission products that are produced in the fuel kernel. However, some fission products, such as silver (Ag) and cesium (Cs), have been observed to escape from intact TRISO particles. Ag release is a major radiological concern due to the long half-life ($\approx$ 250 days) of the ^{110m}Ag isotope.

Previous work performed in the Department of Energy's Nuclear Energy Advanced Modeling and Simulation (NEAMS) program developed a multi-scale approach to predicting the release of Ag from TRISO particles [2]. An effective diffusivity of Ag was calculated for realistic SiC microstructures, which had enhanced Ag diffusivity along grain boundaries (GBs). Density functional theory calculations combined with kinetic Monte Carlo (kMC) simulations were used to determine the bulk diffusivity in the grain interiors, and molecular dynamics (MD) simulations were used to calculate diffusivity along GBs. The GB diffusivity was several orders of magnitude higher than the bulk diffusivty, as expected. Mesoscale simulations were performed using Marmot to determine the effective diffusivities for different microstructures, with bulk and GB diffusivities informed by the atomistic calculations. The SiC grain size in the direction perpendicular to Ag transport was found to have the strongest impact on the effective diffusion coefficient because small grain size in that direction leads to a higher number of GBs in the direction of Ag transport, which acts as high-diffusivity pathways. A function was fit to capture the dependence of diffusivity on grain size both parallel and perpendicular to the transport direction. That function was used in BISON simulations to predict the amount of Ag release in several experiments, and the predictions were compared to those of a model that used an empirically derived Ag diffusivity. Using the multiscale model, the average amount of Ag released in AGR-1 experiments was underpredicted by a factor of approximately 8.5. However, if the effective diffusivity was corrected upward by this factor, the multiscale model predicted the effect of SiC microstructure on total release more accurately that the empirical model.

There are several possible reasons why total Ag release is underpredicted by the multiscale model compared to experiment. One potential cause is the fact that Ag diffusivity in both the grain bulk and GBs may be enhanced by irradiation; the previous modeling work did not account for radiation-enhanced diffusivity. Another potential cause is that multiple types of GBs may be present in the SiC; however, the modeling in Ref. [2] only considered randomly oriented high-misfit GBs.

In this report, simulations are carried out to investigate the effects of radiation-enhanced diffusion and different types of GBs on Ag transport. In Chapter 2, rate theory modeling is used to investigate the effect of irradiation on the bulk diffusivity calculations for Ag in SiC and the impact on Ag release. In Chapter 3, the diffusivity of Ag along a higher-symmetry Σ5 GB was calculated using MD, and the mesoscale model was extended to consider different GBs with different diffusivities. In Chapter 4, preliminary work was performed to investigate SiC GB attack by palladium (Pd) using ab initio MD (AIMD) simulations, which will lay the groundwork for further investigation in Fiscal Year (FY) 2023. Finally, in Chapter 5, conclusions are drawn, and an outlook for further work is given.

2. IRRADIATION EFFECT OF SILVER DIFFUSIVITY IN SILICON CARBIDE

2.1 Rate Theory Modeling of Radiation-enhanced Ag Diffusivity in Bulk SiC

In the previous milestone [2], kMC simulations informed by density functional theory (DFT) calculations were performed to derive the Ag diffusion coefficient in the bulk SiC. The tracer diffusion coefficient of Ag was determined as

$$D_{\mathrm{Ag}}^{\mathrm{eq}} = 2.4 \times 10^{-4} \exp\left(-\frac{5.34 \pm 0.58\ (\mathrm{eV})}{kT}\right)\ (\mathrm{m}^2/\mathrm{s}). \tag{2.1}$$

The calculation was under the assumption that the transport of Ag in the bulk SiC is dominated by the thermodynamic equilibrium concentration of carbon vacancies. This assumption appears reasonable given the high service temperature of TRISO fuels that might allow most of the excess point defects produced by irradiation to reach sinks efficiently, and thus the radiation-enhanced transport of Ag in SiC might not be as important as the thermal diffusion. The calculated thermal diffusion coefficients of Ag show successful application in calculating the effective Ag diffusion coefficient in polycrystalline SiC [3]. Nevertheless, it was found that a correction factor of 8.5 was required to enhance the calculated effective Ag diffusivity to the same level as the empirical value used in BISON. The correction might indicate the potential radiation effect on Ag transport in bulk SiC. The vacancy mobility in SiC is known to be low due to the high migration barrier (3.51 eV). The sluggish vacancy mobility decreases the rate of defect annihilation events, allowing the vacancy concentration to build up under irradiation particularly at a lower range of temperature that leads to radiation-enhanced diffusion. Depending on the rate processes of defects, the dominant diffusion mechanism typically has a transition from thermodynamic diffusion at high temperatures to radiation-enhanced diffusion at low temperatures. However, the transition temperature and the contribution of radiation-enhanced diffusion of Ag in the bulk SiC have never been evaluated. The objective of this section is to predict the radiation-enhanced diffusion of Ag based on existing lower-length-scale data, and the result will then inform and improve the mesoscale and engineering scale simulation capabilities in the following sections.

The radiation-enhanced diffusion coefficient ($D_{\mathrm{Ag}}^{\mathrm{rad}}$) can be expressed as the following form:

$$D_{\mathrm{Ag}}^{\mathrm{rad}} = D_{\mathrm{Ag}}^{\mathrm{eq}} + x_{\mathrm{V}}^{\mathrm{rad}} \frac{D_{\mathrm{Ag}}^{\mathrm{eq}}}{x_{\mathrm{V}}^{\mathrm{eq}}} \tag{2.2}$$

where $D_{\mathrm{Ag}}^{\mathrm{eq}}$ and $x_{\mathrm{V}}^{\mathrm{eq}}$ are respectively the diffusion coefficient of Ag (Eq. 2.1) and vacancy concentration under the thermodynamic equilibrium condition, and $x_{\mathrm{V}}^{\mathrm{rad}}$ is the non-equilibrium vacancy concentration under irradiation. $x_{\mathrm{V}}^{\mathrm{rad}}$ can be determined by the formation energy of a carbon vacancy, which is calculated to be between 4.18 eV (Si-rich) and 4.72 eV (C-rich). Note that based on the MD study of defect production in irradiated SiC showing that carbon vacancies outnumber silicon vacancies in displacement cascades for a wide range of primary knock-on atom (PKA) energies [4], it is reasonably assumed that the radiation-enhanced diffusion of Ag via carbon vacancies will be the dominant vacancy mechanism. Additionally, Eq. 2.2 considers only the vacancy mechanism of Ag transport without the contribution of Ag interstitials. The high formation energy (>10 eV) suggests that Ag interstitials are not energetically favorable to form. Although Ag interstitials could be produced by the kick-out reaction of substitutional Ag by irradiation-produced self-interstitials, the Ag interstitials can quickly be recombined with or trapped by vacancy defects that are produced by irradiation, whose concentration is expected to be significantly higher than that of Ag interstitials. Additionally, due to the fast transport of self-interstitials, these excess point defects can be efficiently annihilated by sinks. The concentration of self-interstitials will thus be significantly less than mobile vacancies, thereby reducing the possibility of the kick-out reactions that produce Ag interstitials. In other words, the high concentration of vacancies and low concentration of self-interstitials in a typical irradiated crystalline system do not favor long range transport of kick-out Ag interstitials.

A rate theory model is used in this study to describe the time dependence of $x_{\mathrm{V}}^{\mathrm{rad}}$ that determines the radiation-enhanced diffusion of Ag. In addition to the recombination and constant sinks that are typically considered in most rate theory studies, the present model also includes the effects of solute trapping and vacancy clustering. This modified rate theory model has been applied in recent studies of radiation-accelerated precipitation in steels [5, 6, 7] and found successful applications. For Ag transport in SiC, the effect of solute trapping can be important because of the strong binding of mobile vacancy by Ag when they do not occupy the same sublattice sites of SiC.

The time dependence of the carbon vacancy and interstitial concentrations in the bulk SiC can be given as

$$\frac{\partial x_{\mathrm{V}}}{\partial t} = G + \frac{x_{\mathrm{tv}}}{\tau_{\mathrm{t}}} - k_{\mathrm{rec}}(D_{\mathrm{I}} + D_{\mathrm{V}})x_{\mathrm{I}}x_{\mathrm{V}} - D_{\mathrm{V}}x_{\mathrm{V}}S_{\mathrm{t}} - \frac{4\pi r_{\mathrm{trap}}}{V_a}D_{\mathrm{V}}x_{\mathrm{V}}x_{\mathrm{trap}} \tag{2.3}$$

$$\frac{\partial x_{\mathrm{I}}}{\partial t} = G - k_{\mathrm{rec}}(D_{\mathrm{I}} + D_{\mathrm{V}})x_{\mathrm{I}}x_{\mathrm{V}} - D_{\mathrm{I}}x_{\mathrm{I}}S_{\mathrm{t}} - \frac{4\pi r_{\mathrm{trap}}}{V_a}D_{\mathrm{I}}x_{\mathrm{I}}x_{\mathrm{tv}} \tag{2.4}$$

where V and I denote vacancies and interstitials respectively. Note that since the dominant point defects in SiC produced by irradiation are carbon vacancies and carbon interstitials [8], the evolution of other point defects, including silicon vacancies, silicon interstitials, and antisite defects, are not considered in the rate theory equations. $G = \xi K_0$ is the defect production rate, ξ is the displacement efficiency and K_0 is the rate of radiation damage in terms of displacements per atom (dpa). $K_0 = \sigma_{\mathrm{dpa}}\phi$, where σ_{dpa} is the dpa cross-section. It is assumed that the bias of the productions of carbon vacancies and carbon interstitials is negligible. The assumption is based on a recent MD study showing that the residual number of carbon vacancies and carbon interstitials in displacement cascades is at the same magnitude [8]. The residual carbon interstitials is about 10% more than carbon vacancies for the PKA energy ranging from 10 to 100 keV. k_{rec} is the coefficient of the recombination rate. Note that the recombination of a carbon interstitial and a carbon vacancy is not a spontaneous reaction but with a reaction barrier E_{rec} about 0.9 eV [9]. By following the steady-state reaction rate

[10], k_{rec} can be expressed as

$$k_{\mathrm{rec}} = \frac{4\pi r_{\mathrm{rec}}}{V_a} \frac{r_{\mathrm{rec}}\beta}{r_{\mathrm{rec}}\beta + 1} \tag{2.5}$$

where r_{rec} is the recombination radius in the bulk matrix, V_a is the atomic volume, and $r_{\mathrm{rec}}\beta \sim \exp(E_{\mathrm{D}} - E_{\mathrm{rec}}/kT)$. E_{D} is the migration barrier of the fast diffusion species involving in the recombination reaction, which in this case is the carbon interstitial. Note that for the spontaneous recombination without reaction barrier, the second fraction term in Eq. 2.5 will be almost equal to 1 and the recombination rate coefficient reduces to the typical expression $k_{\mathrm{rec}} \sim 4\pi r_{\mathrm{rec}}/V_a$.

D_{V} and D_{I} in Eqs. 2.3 and 2.4 are respectively the diffusion coefficients of carbon vacancies and interstitials, r_{trap} is the trap recombination radius, x_{trap} is the trap density, and x_{tv} is the trapped vacancy concentration. S_{t} is the total sink strength, which includes the contributions of dislocations, GBs, and defect clusters:

$$S_{\mathrm{t}} = \rho_d + 3\frac{\sqrt{\rho_d}}{d_{\mathrm{grain}}} + S_{\mathrm{c}} \tag{2.6}$$

where ρ_d is the dislocation density, d_{grain} is the grain size, and S_c is the sink strength from vacancy clusters, also called unstable matrix features. Interstitial clusters and dislocation loops, which can also be produced by irradiation, are not considered in this study. Following [11], the vacancy clusters can be considered as a dilute concentration of spherical temporary sinks created in irradiation-induced displacement cascades. The creation rate of vacancy clusters can be approximated to be proportional to the irradiation flux ϕ and creation cross section σ_c [11]. Vacancy clusters can also be dissolved by emission of vacancies at a rate proportional to the vacancy cluster density (N_c) and the inverse of the characteristic time (τ_c) for vacancy emission from vacancy clusters [11]. The characteristic annealing time can be calculated by Ref.[12] in the following form:

$$\tau_{\mathrm{c}} = \frac{\tau_{\mathrm{c0}}}{\exp\left(-E_{\mathrm{vc}}/kT\right)} \tag{2.7}$$

where τ_{c0} is the pre-factor of the annealing time and E_{vc} is the binding energy of the vacancy clusters. The steady-state number density of vacancy clusters (N_c) can then be derived as $\phi\sigma_c\tau_c/V_a$ [11], which was also applied in a recent model that evaluates radiation enhanced diffusion in reactor pressure vessel steels [5]. By using the standard expression of an individual sink strength for spherical vacancy clusters, $4\pi r_c N_c$ [11], where r_{c} is the capture radius, the steady-state sink strength of vacancy clusters gives [12]:

$$S_{\mathrm{c}} = 4\pi r_{\mathrm{c}}\phi\sigma_{\mathrm{c}}\tau_{\mathrm{c}}/V_a \tag{2.8}$$

τ_{t} in Eq. 2.3 is the characteristic time of solute trapping by a vacancy, which can be expressed as

$$\tau_{\mathrm{t}} = \frac{d^2}{D_{\mathrm{V}}\exp(-E_{\mathrm{b}}/kT)} \tag{2.9}$$

where E_{b} is the binding energy and d is the nearest neighbor distance of the SiC lattice. In this study, $\mathrm{Ag}_{\mathrm{Si}}$ (substitutional Ag atoms at the Si sublattice in bulk SiC) is considered as the impurity type that can trap the mobile carbon vacancies due to the strong binding as predicted by DFT [2]. The predicted binding energy is $\sim 3.0 - 3.5$ eV/atom.

By making the following approximations $D_\mathrm{I} >> D_\mathrm{V}$ and $D_\mathrm{I} x_\mathrm{I} = D_\mathrm{V} x_\mathrm{V}$, the steady-state solution of Eqs. 2.3 and 2.4 can be solved by finding roots of the polynomial. It will be numerically convenient to define the fraction of point defects (vacancies and self-interstitial atoms) that escape recombination to reach sinks as

$$g_\mathrm{s} = \frac{x_\mathrm{V} D_\mathrm{V} S_\mathrm{t}}{G}. \tag{2.10}$$

By placing Eq. 2.10 and the above two approximations into the steady-state condition of Eq. 2.3, g_s can be solved numerically. x_V can be derived by the relation with g_s in Eq. 2.10, and finally the radiation-enhanced diffusion coefficient $D_\mathrm{Ag}^\mathrm{rad}$ can be calculated by Eq. 2.2.

Physical parameters used in this simulation study are summarized in Table 2.1. The AGR-1 irradiation conditions are considered, and the radiation-enhanced diffusion coefficient of Ag will be derived as a function of temperature. Note that some of the parameters are either unknown or have a high uncertainty, so reasonable estimate was made for those parameters, which is marked by * in Table 2.1. For instance, the cross-section of dpa was suggested to stabilize at the magnitude between $\sim 5 \times 10^{-26}$ and 9×10^{-26} dpa/(n m^{-2}), depending on the neutron energy [13]. Since there is no data reporting the dislocation density in SiC in the TRISO particle from the AGR-1 capsule, a typical dislocation density (10^{13} m^{-2}) for crystalline solids is assumed. Other unknown parameters include recombination radii for bulk SiC and traps, as well as the production cross section for vacancy clusters in SiC. These parameters require further lower-length-scale simulations to clarify, and therefore in the present study reasonable values were used for these uncertain parameters.

Table 2.1. Physical parameters used in the rate theory model. The symbol * indicates the parameters that are unknown, uncertain, or the values are within a range of possible variability.

Parameter	Value	Unit	Ref.
Dose rate (AGR-1 condition)	4.70×10^{17}	n m^{-2} s^{-1}	[14]
Dpa cross-section*	8.0×10^{-26}	dpa/(n m^{-2})	[13]
Grain size	0.3×10^{-6}	m	[3]
Dislocation density*	1.0×10^{13}	m^{-2}	
Trap concentration*	1.0×10^{-7}	-	
Recombination barrier (matrix)	0.9	eV	[9]
Binding energy of traps	3.5	eV/atom	[2]
Cascade efficiency	0.7	-	[4]
Carbon vacancy formation energy (C-rich)	4.72	eV	[2]
Carbon vacancy formation energy (Si-rich)	3.18	eV	[2]
Carbon vacancy migration barrier	3.51	eV	[2]
Carbon interstitial migration barrier	0.67	eV	[15]
Carbon vacancy diffusivity pre-factor	9.68×10^{-8}	m^2 s^{-1}	[2]
SiC lattice constant	4.36×10^{-10}	m	
Vacancy cluster binding energy*	3.5	eV/site	
Production cross section for vacancy clusters*	4.5×10^{-29}	m^2	
Recombination radius (matrix)*	3.1×10^{-10}	m	
Recombination radius (trap)*	3.1×10^{-10}	m	

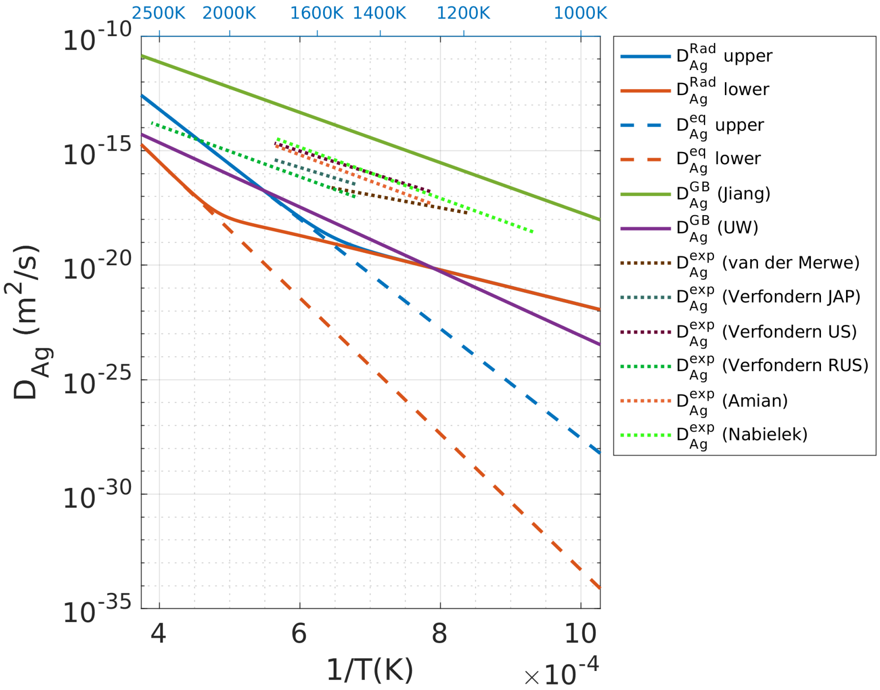

Figure 2.1. Plots showing the diffusion coefficient of Ag in bulk SiC as a function of reciprocal temperature. The solid blue and red lines show the calculated radiation-enhanced diffusion coefficient of Ag in bulk SiC under the AGR-1 conditions. The dashed lines are the thermal diffusion coefficient of Ag under thermodynamic equilibrium of vacancy concentration. The dotted lines are from the diffusion data measured by experiments [17, 18, 19, 20]. The solid green and purple lines are the grain boundary diffusion coefficient of Ag in SiC calculcated by MD [2] and kMC [16], respectively.

Figure 2.1 shows the calculated radiation-enhanced diffusion coefficient of Ag $D_{\text{Ag}}^{\text{rad}}$ in the bulk SiC, along with the calculated diffusion coefficient under thermodynamic equilibrium $D_{\text{Ag}}^{\text{eq}}$ [2], the calculated GB diffusion coefficient $D_{\text{Ag}}^{\text{eq}}$ by MD and kMC simulations [2, 16], as well as the Ag diffusion coefficient reported by experimental studies of integral release measurement [17, 18, 19, 20]. The difference of blue and red lines in the plots of $D_{\text{Ag}}^{\text{eq}}$ and $D_{\text{Ag}}^{\text{rad}}$ is caused by the difference of carbon vacancy formation energy for C-rich and S-rich SiC. The calculation result of $D_{\text{Ag}}^{\text{rad}}$ shows that the transition from thermal diffusion to radiation-enhanced diffusion of via carbon vacancies happens at the temperature between 1500K and 2100 K. The blue and red $D_{\text{Ag}}^{\text{rad}}$ lines converge to a single line when the temperature is lower than ∼1600K, at which the Ag transport will be mostly mediated by the radiation-induced point defects instead of thermally activated vacancies at the low temperatures. The result suggests that radiation-enhanced transport of Ag in SiC may still matter during the service condition of TRISO fuels. Note that the calculated $D_{\text{Ag}}^{\text{rad}}$ is still 1-3 orders of magnitude lower than the experimental data, and the experimental data (dotted lines) does not show the evident transition of diffusion mechanisms as $D_{\text{Ag}}^{\text{rad}}$ does. These comparisons indicate that GB diffusion of Ag may still be the dominant transport mechanism.

Although the transition of diffusion mechanisms was not observed in the experiments of Ag transport in SiC, it was found for different fission product species (such as Sr and Cs) in SiC, as suggested by the data in Figure 2.2 showing

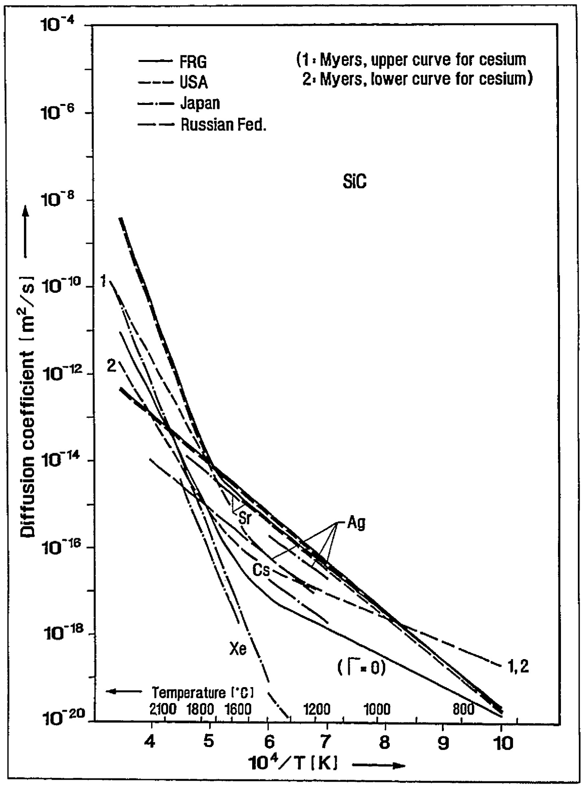

Figure 2.2. Plots showing the diffusion coefficients of fission products in SiC as a function of reciprocal temperature. This figure is from Ref. [18].

the change of Arrhenius trends from high to low temperatures [18]. For Cs transport, the transition temperature was suggested to occur between 1473K and 1873K, which is similar to the prediction for Ag in this study. In Figure 2.2, the reduced slope as temperature decreases suggests the transition of the dominant diffusion mechanism to that with lower activation energy. This trend indicates that the diffusion process may involve radiation-induced defects more at low temperatures compared to the thermal diffusion, and therefore the activation energy does not include the contribution of thermally-activated defect formation. An alternative and additional mechanism associated with the transition is the preferred GB diffusion at low temperatures. An atomistic simulation of Cs diffusion in SiC shows that GB diffusion of Cs dominates the bulk diffusion, while at the same time the study suggests that radiation-enhanced bulk diffusion may be responsible in irradiated SiC [21]. Given the uncertainty of energetics involving defects and fission products as well as the lack of experimental data characterizing and quantifying the evolution of extended defects (e.g., dislocation loops, network dislocations, GBs, and mixed defect clusters), a comprehensive investigation is challenging. It would be valuable to perform integrated experimental and computational investigation to confirm and clarify the contribution of various transport mechanisms and the relationship with defect evolution under irradiation.

To demonstrate how microstructure and defect energetics affect the Ag transport in the bulk, Figure 2.3 (a)–(d) show the effects of grain size, dislocation density, trapping density or fraction, and vacancy cluster binding energy on

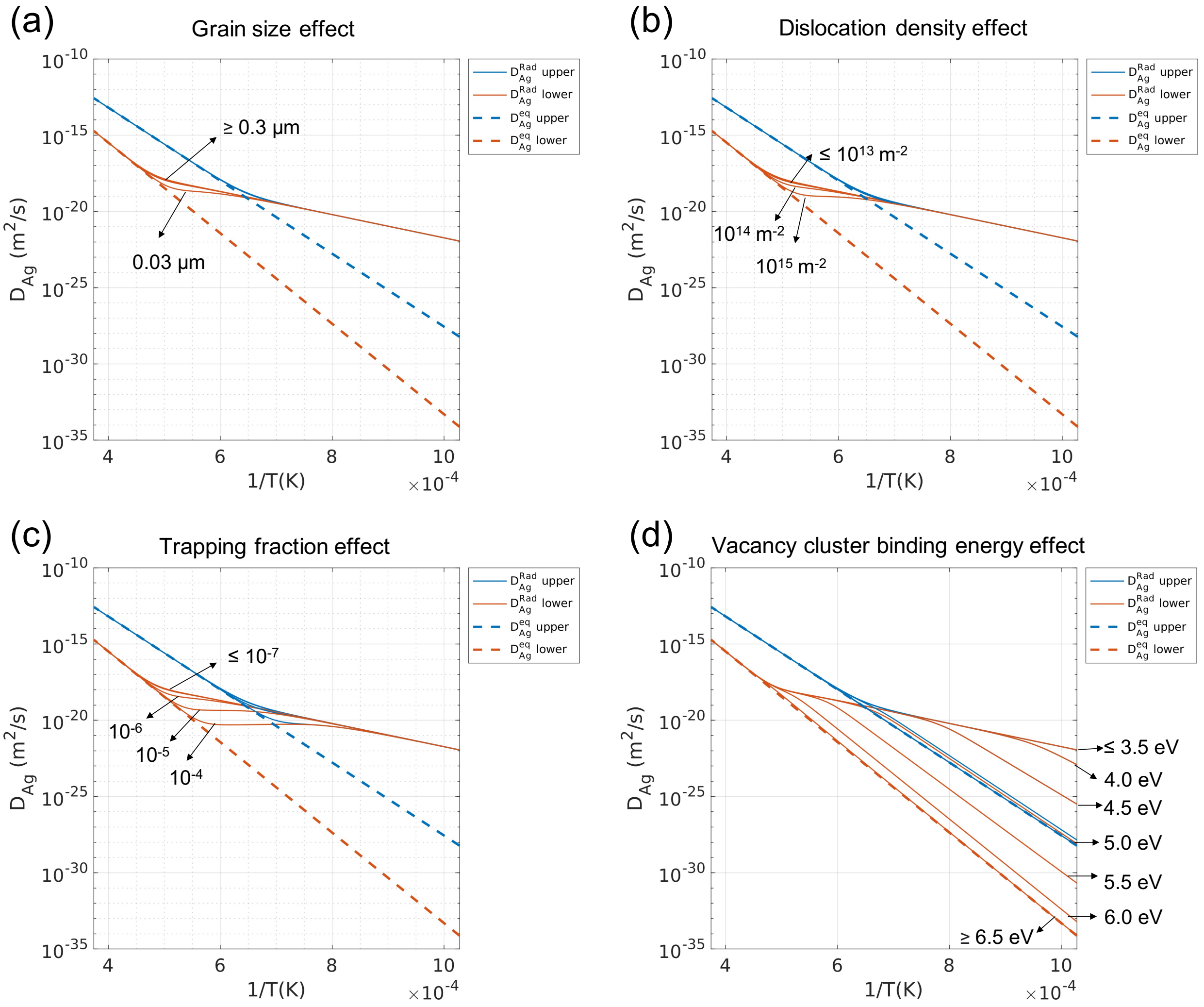

Figure 2.3. Plots showing the effects of (a) grain size, (b) dislocation density, (c) trapping fraction, and (d) vacancy cluster binding energy on the diffusion coefficients of Ag in bulk SiC as a function of reciprocal temperature.

the diffusion coefficient of Ag in bulk SiC. The parameters that are not mentioned are the same as those listed in Table 2.1. Generally, increasing the sink or trap density decreases $D_{\mathrm{Ag}}^{\mathrm{rad}}$ and such the effect appears more pronounced for the trapping fraction than dislocation density or grain size, as shown in 2.3 (a)– (c). Note that while the grain size appears to have minor influence on the bulk diffusion, it can modify significantly the effective Ag transport in polycrystalline SiC, which will be shown in the next section. Figure 2.3 (d) shows the significant effect of the vacancy cluster binding energy E_{vc} on the radiation-enhanced Ag diffusion. Increasing E_{vc} from 3.5 to 4.0 eV results in decrease of $D_{\mathrm{Ag}}^{\mathrm{rad}}$ particularly starting from the low-temperature end (~1000K), which will extend to the higher temperature as E_{vc} increases further. The effect of radiation-enhanced diffusion will almost vanish as E_{vc} reaches higher than 6.5 eV.

One major limitation of the model presented in this section is the simplified treatment of solute-defect complexes, including just carbon vacancies, interstitials, trap impurities, and formation of carbon vacancy clusters. Although it has been indicated by MD studies that carbon vacancies and carbon interstitials are the dominant residual point defects under irradiation, it remains to be clarified how a wide variety of point defects interacts with the fission products such as Ag in the bulk SiC that may form mixed complexes. These mixed complexes might act as traps that reduce the mobility of points defects or fission products, or they can be mobile and act as carriers for fission product transport, depending on their mobility and stability. Comprehensive modeling and simulation of these complex interactions and reactions require robust descriptions of interatomic energies with ab initio accuracy. Specifically, a combination of atomistic, mean-field, and coarse-grained approaches will be important to capture these cluster reactions and parameterize rigorous mesoscale models. This integrated approach is currently out of scope for this FY.

2.2 Fitting Lower Length Scale Simulations Results to be Used at the Mesoscale

The irradiation-enhanced Ag diffusivity in bulk SiC has been quantified using DFT and kMC calculations in Section 2.2. To incorporate irradiation effects at the mesoscale, it is necessary to fit the results provided in Figs. 2.1 and 2.3 and define Ag diffusivity in bulk SiC as a function of temperature and flux. Note that at the mesoscale, we use the bulk diffusivity obtained for a grain size of 0.3 microns, a vacancy cluster binding energy of 3.5 eV/sites, a trapping fraction of 1×10^{-7}, and a dislocation density of 1×10^{-13}. For a given flux, Figs. 2.1 and 2.3 shows that thermal effects dominate diffusion at higher temperatures, while irradiation-enhanced mechanisms become important at lower temperatures. Ag diffusivity in bulk SiC is therefore described as

$$D_{bulk}(T, F) = D^{th}(T) + D^{irr}(T, F) \tag{2.11}$$

with T the temperature in K, F the flux in n/m^2/s, $D^{th}(T)$ the diffusivity due to thermal effects in m^2/s, and $D^{irr}(T, F)$ the diffusivity due to irradiation effects in m^2/s. $D^{th}(T)$ is defined in Refs. [2, 3] as

$$D^{th}(T) = D_0^{th} \exp\left(\frac{-Q^{th}}{RT}\right) \tag{2.12}$$

with $D_0^{th} = 2.4 \times 10^{-4}$ m^2/s and $Q^{th} = 459 \times 10^3$ J/mol. To define $D^{irr}(T, F)$, a Python script was developed to identify the change of slope due to irradiation-enhanced diffusivity and then was fitted to the low temperature regime at different fluxes with an Arrhenius law, following

$$D^{irr}(T, F) = D_0^{irr}(F)\left(\frac{-Q^{irr}(F)}{RT}\right). \tag{2.13}$$

The effect of flux on D_0^{irr} and Q^{irr} and the corresponding fits are illustrated in Fig. 2.4. $D_0^{irr}(F)$ has been shown to increase with flux level as

$$D_0^{irr}(F) = a\left(\frac{F}{F_0}\right)^b \tag{2.14}$$

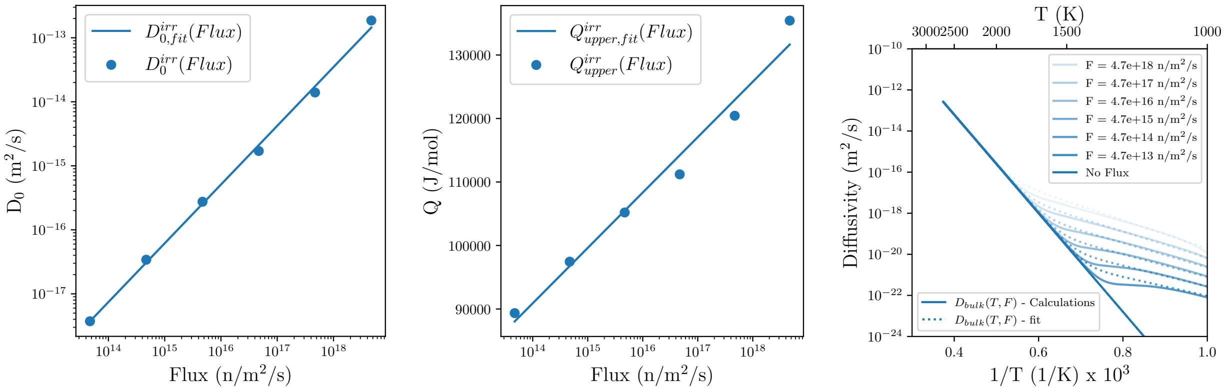

(a) $D_0^{irr}(F)$ (b) $Q^{irr}(F)$ (c) $D_{bulk}(T,F)$

Figure 2.4. Fitting the irradiation-enhanced diffusion as a function of flux. (a) shows how D_0^{irr} evolves with the flux and how it was fitted using Eq. (2.14), and (b) shows how Q^{irr} evolves with the flux and how it was fitted using Eq. (2.15). (c) shows the final fit for $D_{bulk}(T,F)$ described in Eq. (2.11).

where $F_0 = 1$ n/m^2/s ensures that F/F_0 is dimensionless, $b = 0.9177$ (-), and $a = 1.056 \times 10^{-30}$ m^2/s. The quality of this fit between $F = 4.7 \times 10^{13}$ n/m^2/s and $F = 4.7 \times 10^{18}$ n/m^2/s is quantified by $R^2 = 0.998$. $Q^{irr}(F)$ has been defined as

$$Q^{irr}(F) = c \ln(F) + d \tag{2.15}$$

with $c = 3788$ J/mol and $d = -31216$ J/mol. The quality of this fit between $F = 4.7 \times 10^{13}$ n/m^2/s and $F = 4.7 \times 10^{18}$ n/m^2/s is quantified by $R^2 = 0.977$. Both these fits (i.e., Eqs. (2.14) and (2.15)) are shown in Fig. 2.4.

The fit of the bulk diffusion proposed in this section accurately captures the two different regimes (i.e., the thermal diffusion at higher temperatures and the irradiation-enhanced diffusion at lower temperatures). However, the Ag bulk diffusivity is slightly overestimated around transition temperatures, although not by an amount significantly greater than the uncertainty. This fit will be used in the rest of the section to describe the irradiation-enhanced Ag diffusion in bulk SiC.

2.3 Irradiation Effects on Effective Ag Diffusivity in SiC at the Mesoscale

2.3.1 Description of the SiC microstructures

The mesoscale simulations were performed in a similar fashion as in Refs. [2, 3]. The same polycrystalline structures generated using Ref. [22] and described in Refs. [2, 3] were used. They are 2D domains of dimensions 9 μm × 9 μm generated with the desired grain sizes, grain aspect ratios, and GB widths. Their grain major axis varies from 0.75 μm to 3 μm, and the grain minor axis varies from 0.3 μm to 0.82 μm. Although the GB size of the polycrystalline SiC is approximately equal to 1 nm, with variations between high-angle GBs (HAGB) and low-angle GBs (LAGB), the GB width is scaled up to 60 nm using the approach described in Refs. [2, 3] to limit computational costs. As discussed in

Refs. [2, 3], the simulated microstructures cover the variations in grain dimensions found in the AGR-1 and AGR-2 fuel batches, hence providing results relevant for realistic SiC grain sizes for TRISO fuel particles.

It is important to note that, as in Refs. [2, 3], the polycrystalline structures used in this section have continuous interfaces. Grains are described using a set of N order parameters η_{Gr_i} with $i \in [1, N]$ [23]. A given order parameter is equal to 1 in a given grains, and equal to 0 in neighboring grains, with a continuous transition from 1 to 0 at the GB. The GBs can be described by

$$\chi = \sum_{i}^{N} \eta_{Gr_i}^2. \tag{2.16}$$

χ is equal to 1 in the grain interior and continuously transitions to 0.5 along the mid plane of the GBs. Based on this continuous description of the grain structure, the diffusion coefficient is defined as

$$D = (1 - h_{GB})D_b + h_{GB}D_{GB} \tag{2.17}$$

with h_{GB} an interpolation function equal to 1 in the GBs and equal to 0 in the grain interior. In this work, h_{GB} was defined as

$$h_{GB}(\chi) = 1 - \frac{1}{2}\left(1.0 + \tanh\left((\chi - \chi_0)\frac{2\tanh^{-1}(0.8)}{\Delta}\right)\right) \tag{2.18}$$

with χ_0 the point at which $h_{GB}(\chi_0) = 0.5$ and Δ the distance $|\chi_{0.9} - \chi_{0.1}|$ for $h_{GB}(\chi_{0.1}) = 0.1$ and $h_{GB}(\chi_{0.9}) = 0.9$. This specific interpolation was used to ensure that the diffusion was the same everywhere in the GBs, including at triple junctions. Other common interpolation functions are often equal to values lower than one at triple junctions, which artificially slows down diffusion. The parameters χ_0 and Δ need to be selected to maximize Δ (i.e., the smoothness of the slope) while ensuring $|h_{GB}(0.5) - 1| \leq tol_{GB}$ and $|h_{GB}(1) - 0| \leq tol_{bulk}$. Although the tolerances tol_{GB} and tol_{bulk} were fixed equal to 10^{-4} in Refs. [2, 3], they actually need to be defined as a function of the ratio of bulk and GB diffusivity. The local diffusivity D defined in Eq. (2.17) should be equal to D_b in the bulk and equal to D_{GB} at GBs. In the bulk, this means that we need to enforce $tol_{bulk} << D_b/D_{GB}$ and $tol_{bulk} << 1$. At GBs, this translates into $tol_{GB} << D_{GB}/D_b$ and $tol_{GB} << 1$. Assuming D_{GB} ranges from 10^{-12} to 1×10^{-18} between 2000 and 1000 K [2, 3], and D_b ranges from 1×10^{-15} to 1×10^{-26} between 2000 and 1000 K (see Fig. 2.4 and Refs. [2, 3]), we get: $tol_{bulk} << D_b/D_{GB} = 1 \times 10^{-8} << 1$, and : $tol_{GB} << 1 << D_{GB}/D_b = 1 \times 10^{3}$. So we can reasonably use $tol_{bulk} << 1 \times 10^{-9}$ and $tol_{GB} = 1 \times 10^{-3}$. This leads to $\chi_0 = 0.625$ and $\Delta = 0.0795$, which differ from the values previously used in Refs. [2, 3], which unfortunately did not ensure $tol_{bulk} << D_b/D_{GB}$, meaning that the bulk diffusivity was overestimated due to the error introduced by the interpolation function in Eq. (2.17).

2.3.2 Effective diffusivity calculations

As in Refs. [2, 3], we use the asymptotic expansion homogenization (AEH) method described in Ref. [24] to determine the effective diffusivity coefficient at the mesoscale. This method is already implemented in Multiphysics Object Oriented Simulation Environment (MOOSE) [25, 26, 27], making it possible to determine effective material properties in a domain with periodic boundary conditions. In the current work, the polycrystals were created with periodic boundary conditions, and the temperature is considered constant across the entire domain. This method can therefore be applied. Simulations are performed for all 20 microstructures. Temperatures range from 1000 K to 2200 K with 200 K increments, which significantly increases the temperature range from Refs. [2, 3] (1450 K to 2073 K) toward AGR-1 and AGR-2 relevant temperatures. In the simulations presented in this work, the flux equals 0, 4.7×10^{13} n/m^2/s, 4.7×10^{14} n/m^2/s, 4.7×10^{15} n/m^2/s, 4.7×10^{16} n/m^2/s, 4.7×10^{17} n/m^2/s, and 4.7×10^{18} n/m^2/s. This covers a wide range of flux around the relevant AGR-1 and AGR-2 flux values [14].

2.3.3 Effective diffusivity calculations

The simulation results for the microstructures and irradiation conditions described in Section 2.3.2 need to be fitted to derive the effective Ag diffusion as a function of temperature, flux, and grain size. The first step is to fit the thermal contribution to the diffusion. The data obtained for a null flux is therefore fitted using the approach developed in Refs. [2, 3]. For each microstructure, the temperature-dependent effective diffusivity is fitted to an Arrhenius equation to obtain a pre-exponential factor D_0 and an energy barrier Q for each microstructure. These coefficients are presented in Fig. 2.5, where they are described as functions of grain major and minor axis length. As in Refs. [2, 3], we found that the grain major axis length does not have a significant influence on D_0 or Q. However, both can be described as linearly dependent on the grain minor axis length. The strong effect of the grain minor axis length is explained by the fact that smaller grains along the minor axis (i.e., the axis perpendicular to the direction of diffusion) mean a higher density of GBs for the Ag to diffuse through, therefore increasing the effective diffusivity of the SiC layer. This is extensively discussed in Refs. [2, 3]. The thermal contribution to the effective Ag diffusivity in SiC as a function of temperature (from 1000 K to 2200 K) and grain size (minor axis from 0.3 μm to 0.82μm) can therefore be described as

$$D^{eff,th}(T, m_i) = \left(D_{m,0} + m_i D_{m,1}\right) \exp\left(-\frac{Q_{m,0} + m_i Q_{m,1}}{RT}\right) \tag{2.19}$$

with T in Kelvin, $R = 8.315$ J/K/mol, m_i in μm, $D_{m,0} = 4.64\times10^{-10}$ m^2/s, $D_{m,1} = -3.15\times10^{-4}$ m/s, $Q_{m,0} = 211\times10^3$ J/mol, and $Q_{m,1} = 5.50 \times 10^9$ J/mol/m. The quality of the fit for the pre-exponential factor and the energy barrier are equal to $R^2 = 0.954$ and $R^2 = 0.991$, respectively. As expected, the coefficients are slightly different than in Refs. [2, 3] since the temperature range and interpolation function (i.e., Eq. (2.18)) have been updated.

In this work, the total effective Ag diffusivity in SiC is defined as

$$D^{eff,tot}(T, F, m_i, m_a) = D^{eff,th}(T, m_i) D^{eff,irr}(T, F, m_i, m_a) \tag{2.20}$$

with $D^{eff,th}(T, m_i)$ derived in Eq. (2.19), and $D^{eff,irr}(T, F, m_i, m_a)$ the irradiation-enhanced contribution to the effective diffusivity. Using the values for $D^{eff,tot}$ provided by the mesoscale simulations, and $D^{eff,th}(T, m_i)$ provided by Eq. (2.19), we can derive $D^{eff,irr}(T, F, m_i, m_a)$ as a function of temperature, flux, and grain minor and major axis lengths, as shown in Fig. 2.6 To fit the data shown in Fig. 2.6, $D^{eff,irr}(T, F, m_i, m_a)$ is defined as

$$D^{eff,irr}(T, F, m_i) = 1 + D_{irr,0} \left(\frac{F}{F_0}\right)^{D_{irr,1}} \left(1 + D_{irr,2} m_i\right) \exp\left(\frac{D_{irr,3}}{T}\right), \tag{2.21}$$

with $F_0 = 1$ n/m^2/s ensuring that F/F_0 is adimensional. $D^{eff,irr}$ is therefore linearly dependent on the grain minor

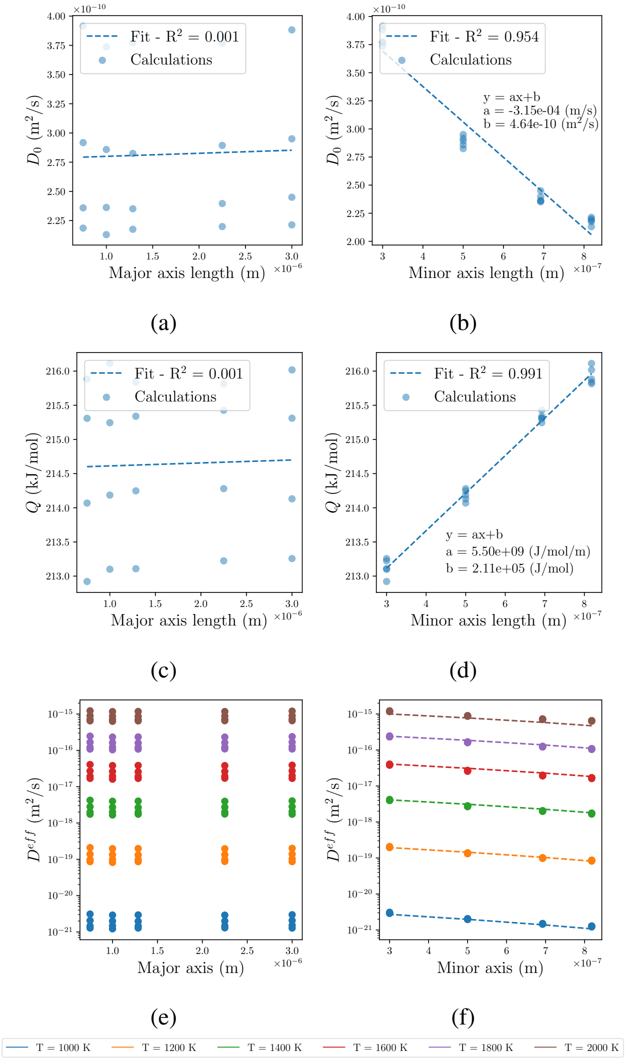

(a) (b)

(c) (d)

(e) (f)

Figure 2.5. Derivation of the thermal contribution to the effective Ag diffusion coefficient as a function of the temperature T, the grain minor axis length m_i, and the grain major axis length m_a. (a,b) show how D_0 depends on (a) m_a and (b) m_i, and (c,d) show how Q depends on (c) m_a and (d) m_i. In (a,c), the points provided for one m_a value correspond to the different minor axis lengths. Similarly, in (b,d), the points provided for a given value of m_i corresponds to the different major axis lengths. While both D_0 and Q are independent of m_a, D_0 seems to slightly decrease with increasing m_i, and Q increases linearly with m_i. (e,f) show how the thermal contribution to the effective diffusion coefficient $D^{eff,th}$ depends on (e) m_a and (f) m_i for different temperatures. The best fit, which successfully captures the temperature and microstructure effects on $D^{eff,th}$, was also added in (f).

axis length, increases exponentially with the inverse of the temperature, and evolves as a power law with respect to the flux. Note that, just like $D^{eff,th}(T, m_i)$, $D^{eff,irr}$ seems to be independent of the grain major axis length, which is visible in Fig. 2.6 and translated into Eq. (2.21). The coefficients $D_{irr,i}$ are optimized using the root mean square

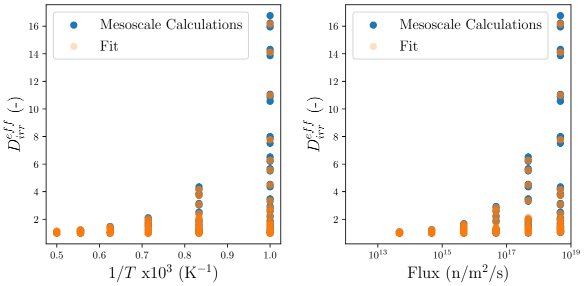

(a) Temperature (b) Flux

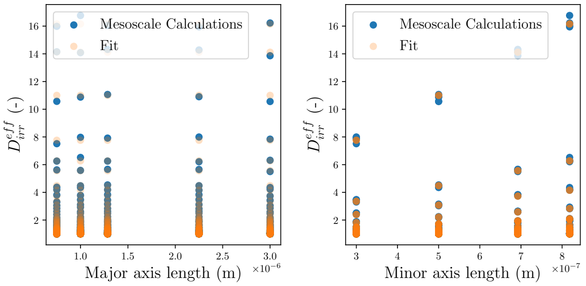

(c) Grain major axis length (d) Grain minor axis length

Figure 2.6. Influence of (a) temperature, (b) flux, and (c,d) grain major and minor axis lengths on the irradiation-enhance diffusion contribution in polycrystalline SiC microstructures. While the grain major axis length does not seem to influence $D^{eff,irr}$, the effect of temperature, flux, and grain minor axis length is accurately captured in Eq. (2.21), as shown by the match between data points from mesoscale calculations and the model's predictions.

error with the available data, which leads to: $D_{irr,0} = 4.23 \times 10^{-13}$ (n/m^2/s)$^{-1}$, $D_{irr,1} = 0.458$ (-), $D_{irr,2} = 8.53 \times 10^6$ m^{-1}, and $D_{irr,3} = 9.42 \times 10^3$ K^{-1}. It is remarkable that for thicker grains, and at $T = 100$ K, the irradiation-enhanced diffusion in bulk SiC can increase the effective Ag diffusion by a factor of 16 (see Fig. 2.6).

Equations (2.19) to (2.21) define the total effective Ag diffusivity, accounting for both thermal diffusion and irradiation-enhanced contribution, as a function of temperature, flux, and grain size. $D^{eff,tot}(T, F, m_i)$ is shown in Fig. 2.7, and while thermal effects dominated the high-temperature regime, irradiation-enhanced diffusion is visible at lower temperatures. The effective Ag diffusion coefficient derived through atomistic and mesoscale calculations falls close to the empirical value currently used in BISON. As detailed above, the total effective Ag diffusivity has been defined for temperatures ranging from 1000 to 2200 K, for flux ranging from 0 to 4.7×10^{18} n/m^2/s, and grain minor axis length between 0.3 μm and 0.82 μm. The effective Ag diffusion coefficient derived through atomistic and mesoscale calculations falls close to the empirical value currently used in BISON. Multiplying $D^{eff,tot}$ by a correction factor $\delta_{corr} = 10$ is needed to increase the calculated effective Ag diffusivity to a similar level than the empirical value used in BISON while still accounting for the effect of the microstructure and irradiation. We define

$$D_{corr}^{eff,tot}(T, F, m_i) = \delta D^{eff,tot}(T, F, m_i) \tag{2.22}$$

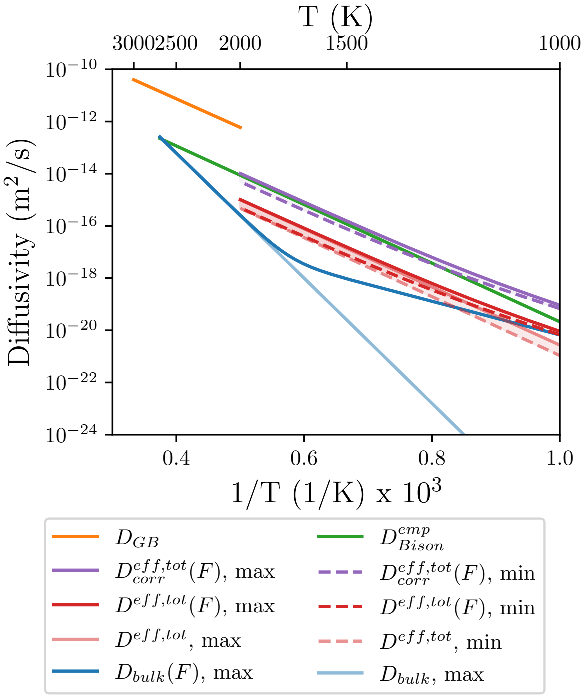

Figure 2.7. Comparison of the Ag diffusion coefficients provided by atomistic simulations (i.e., the temperature and irradiation-dependent bulk D_{bulk} derived in Section 2.1 and the GBs D_{GB} [2]), the empirical coefficient D^{emp}_{BISON} previously used in BISON provided in Refs. [28, 29, 1, 30], and the effective diffusivity values provided by the current mesoscale study $D^{eff,tot}$ (Eqs. (2.19) to (2.21)). The different values for $D^{eff,tot}$ at each temperature correspond to the extreme grain minor axis length values of the SiC microstructures described in Section 2.3.1 (full line for smallest minor axis size, dotted lines for largest minor axis size), and different flux values ($D^{eff,tot}$ for 0 flux, $D^{eff,tot}(F)$ for flux = 4.7×10^{17} n/m^2/s). The irradiation-enhanced diffusion is visible at low temperatures. The effective Ag diffusion coefficient derived through atomistic and mesoscale calculations falls close to the empirical value currently used in BISON. Multiplying $D^{eff,tot}$ by a correction factor $\delta_{corr} = 10$ is needed to increase the calculated effective Ag diffusivity to the same level than the empirical value used in BISON while still accounting for the effect of the microstructure and irradiation, as shown by $D^{eff,tot}_{corr}$, Eq. (2.22).

the corrected version of the effective Ag diffusivity derived in Eqs. (2.19) to (2.21). Note that with $\delta_{corr} = 10$, the diffusivity at lower temperatures is higher with the mechanistic model developed in this study than with the empirical diffusivity.

2.4 Simulations of AGR-1 Ag Release Measurements

The effective Ag diffusivity derived in the previous section has been implemented in the fuel performance code BISON to study the effect of microstructure and irradiation levels on Ag release from TRISO particles. To that end, the time-

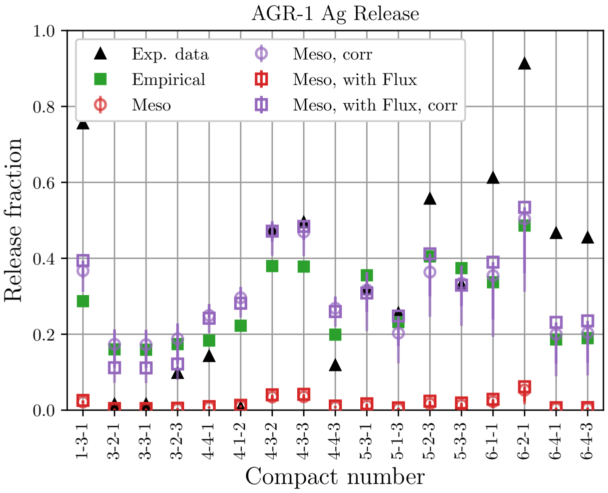

Figure 2.8. Comparison of measured (post-irradiation examination (PIE)) and computed (BISON) Ag release fractions for AGR-1 compacts. The BISON results show the values obtained with the empirical BISON diffusivity from Refs. [1, 30, 29, 28] (green), as well as the results obtained by the current study with the new mesoscale effective Ag diffusion coefficient (red) and the corrected version (purple). The color code is the same as in Fig. 2.7, but empty circles show the predictions for 0 flux, whereas empty squares show the model's predictions accounting for irradiation effects. The ranges shown for the mesoscale diffusion coefficient correspond to the minimum and maximum grain minor axis size for each as-fabricated compact provided in Ref. [2, 3], and the markers correspond to the optimized values. When using $D^{eff,tot}$, the predicted Ag release fraction is often significantly underestimated, except for compacts 3-2-1, 3-3-1, and 4-1-2. However, using $D^{eff,tot}_{corr}$ improves the predicted Ag release fraction in the large majority of cases. Including the effect of the microstructure on Ag diffusion provides more flexibility to the model. As expected, accounting for irradiation effects increases Ag release, but this effect is limited.

dependent flux was derived from the fluence history, already available in BISON for each AGR-1 capsule. Simulations were performed both with and without irradiation effects and both with and without the correction factor introduced in Eq. (2.22). The predictions are shown in Fig. 2.8.

When using $D^{eff,tot}$, the predicted Ag release fraction is often significantly underestimated, except for compacts 3-2-1, 3-3-1, and 4-1-2. However, using $D^{eff,tot}_{corr}$ improves the predicted Ag release fraction in the large majority of cases. Including the effect of the microstructure on Ag diffusion provides more flexibility to the model. As expected, accounting for irradiation effects increases Ag release, but this effect is limited.

2.5 Discussion

A new effective Ag diffusivity in SiC has been developed using a multi-scale and mechanistic approach. The new diffusivity accounts for temperature, grain size, and irradiation effects. The inclusion of the irradiation effect is the novelty of this study and is most important at temperatures below 1500 K. An important thing to note is that the irradiation effect is a function of flux, not fluence. The reason is that bulk irradiation-enhanced diffusivity is not expected to last after irradiation stops.

The new effective Ag diffusivity has been used to model Ag release from TRISO fuel particles, and its predictions were compared against PIE data from AGR-1. The predictions accounting for microstructure and irradiation effects better match the experimental measurements than an empirical diffusivity. However, the effect of irradiation-enhanced diffusion on Ag release are limited.

The current model, and in particular the correction factor, could be further tuned by calibrating the model against AGR-1 and AGR-2 PIE data. Moreover, other aspects could have a significant effect on Ag diffusion in SiC, namely the fact that Ag can diffuse at different speeds in different GB types, which is studied in Chapter 3, and the potential effect of Pd attack on the SiC layer, therefore influencing Ag diffusivity, which has been studied at lower length scales in Chapter 4.

3. EFFECTS OF GRAIN BOUNDARY TYPES ON SILVER DIFFUSIVITY IN SILICON CARBIDE

In this section, the GBs in the network are divided into two kinds of GB types by the misorientation angle; GBs with a misorientation angle lower than 15° are defined as LAGB, and the others are defined as HAGB. The GB types affect Ag diffusivity because of the different ordering of different GB types [31]. Due to their lower ordering, HAGBs are expected to promote faster diffusion than LAGB. Figure 3.1 (a) and (b) show examples of LAGB and HAGB microstructures in layer-stacked 2D polyimine. We developed a Ag diffusion model with different GB types to accurately predict their influence on Ag release.

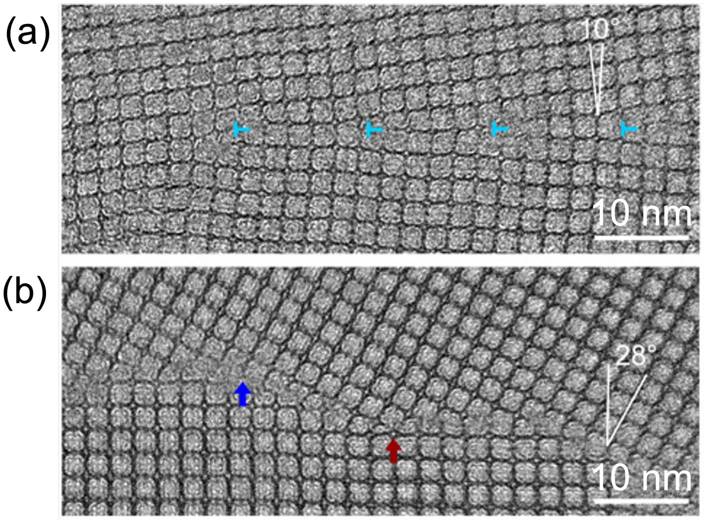

Figure 3.1. Visualization of two grain boundary types in layer-stacked 2D polyimine by Aberration-Corrected High-Resolution Transmission Electron Microscopy imaging: (a) is a LAGB (10°), and (b) is a HAGB (28°) [32].

The section is organized as follows. In Section 3.1, we describe MD simulations that provide Ag diffusivities in both HAGB and LAGB. In Section 3.2, we describe a new feature developed in MOOSE to read a polycrystalline structure, determine the GB types, and assign different diffusivities to the bulk and different GB types. The feature is verified using simple polycrystals: one with three parallel grains and one with triple junctions between grains. Section 3.3 then concludes this section and describes future work.

3.1 Molecular Dynamics Simulation of Ag Diffusion in SiC in Different Grain Boundary Types

We have performed MD simulations using the LAMMPS code [33] and our newly developed analytical bond-order potential to predict the Ag diffusivity along the Σ5 (210)/[001] GB of SiC (see Figure 3.2). In our simulation cell, the Z-axis is perpendicular to the GB plane, the X-axis is parallel to the GB tilt axis, and the Y-axis is parallel to the GB period. Each cell is first relaxed using MD simulations in the NPT (constant number of atoms, pressure, and temperature) ensemble for 10 ps. The mean squared displacement (MSD) data of Ag atoms (up to 10 ns) are obtained using MD simulations in the NVT (constant number of atoms, volume, and temperature) ensemble (see Figure 3.3), based on which the Ag diffusivity is calculated using the Einstein relation.

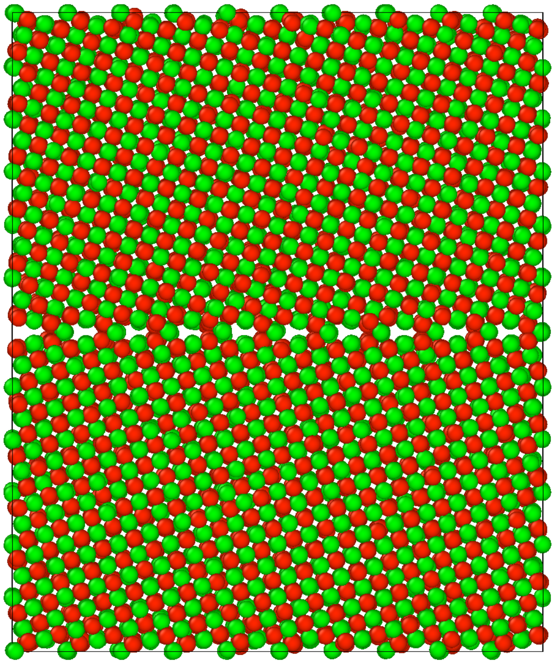

Figure 3.2. Σ5 (210)/[001] GB of SiC. The green and red spheres represent Si and C atoms, respectively.

Our final calculated Ag diffusivity data within the Σ5 (210)/[001] GB of SiC over a wide temperature range from 1750 to 2750 K are shown in Figure 3.4. By fitting our MD results to the Arrhenius equation, we have obtained the following equations to describe the temperature-dependent diffusivity of Ag along X and Y directions within the GB plane:

$$D_{Ag}^{X} = 4.203 \times 10^{-10} \exp\left(-\frac{0.593}{k_B T}\right) \tag{3.1}$$

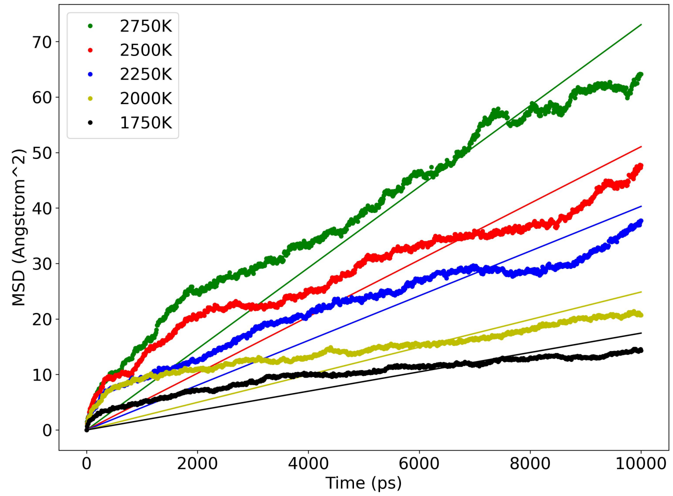

(a) MSD along X-axis

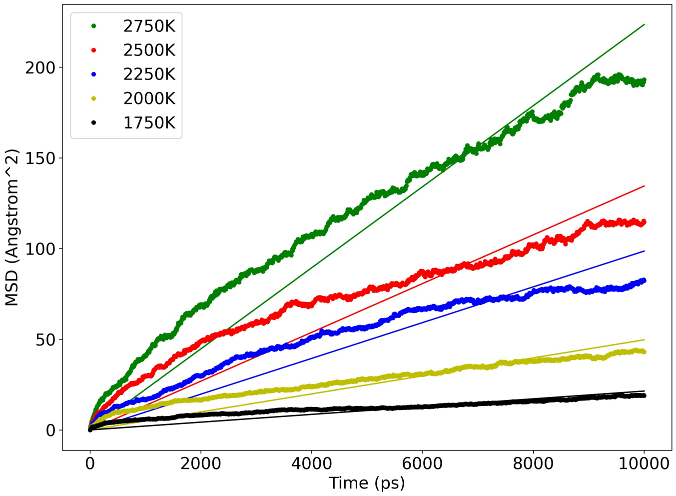

(b) MSD along Y-axis

Figure 3.3. MSD data for Ag atoms diffusing within the Σ5 (210)/[001] GB of SiC at various temperatures. The solid lines represent linear fitting of MSD vs. time data.

$$D_{Ag}^{Y} = 6.161 \times 10^{-9} \exp\left(-\frac{0.954}{k_B T}\right) \tag{3.2}$$

where k_B is the Boltzmann constant. For the Σ5 (210)/[001] GB of SiC, it can be seen that Ag diffusion along the GB period (Y-axis) is faster than along the tilt axis (X-axis). Ag diffusion along both directions are nevertheless significantly faster than along random GBs, which was investigated in the previous milestone [2].

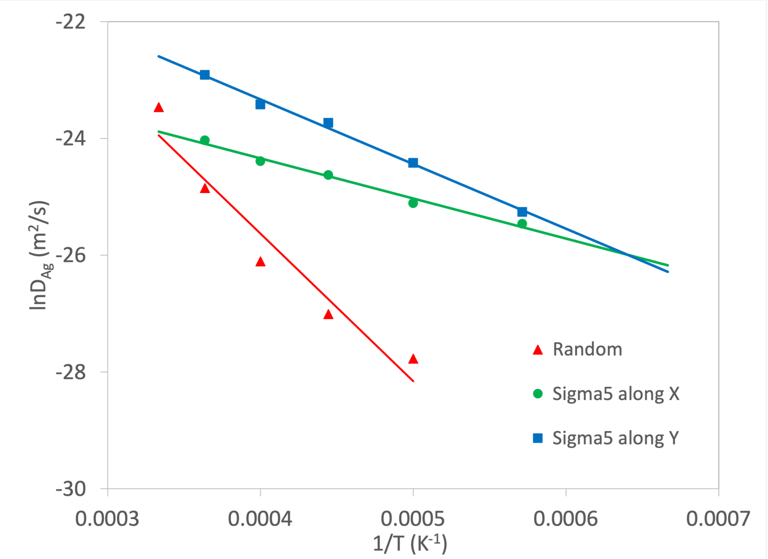

Figure 3.4. Arrhenius plot for Ag diffusivity within the Σ5 (210)/[001] GB of SiC. The solid lines represent the best fitting of MD data using the Arrhenius equation.

3.2 Accounting for Different Grain Boundary Types at the Mesoscale

The diffusion model published in Refs. [2, 3] regards all GBs as HAGBs, all with the same Ag diffusivity. However, a real microstructure would include numerous GB types, which would all have different Ag diffusivity values. This simplification might therefore affect the accuracy of the calculated effective Ag diffusivity in SiC. In this new approach, the Ag diffusivity in SiC GBs depends on the misorientation angle between the neighboring grains. To make the diffusion model more accurate, the GBs are divided into two GB types: LAGBs and HAGBs, based on whether the misorientation is below (LAGB) or higher (HAGB) 15°. To determine the GB type of each GB and then attribute different diffusivities to the bulk, LAGBs, and HAGBs, a new feature is added in MOOSE [25, 34, 27]. The feature can be divided into two phases: GB type determination and local diffusivity assignment. This new feature is described in the MOOSE documentation.

3.2.1 GB misorientation calculations for EBSD data

The first step of this approach is to automatically calculate the GB misorientation in a polycrystalline structure, based on the grain orientations. The grain orientation is determined from electron backscatter diffraction (EBSD) measurements, and the misorientation of all possible GBs is calculated, accounting for the symmetries of cubic materials.

3.2.1.1 Implementation for misorientation calculation

For two grains A and B with different grain orientations g_A and g_B, their misorientation Δg is defined as

$$\Delta g = (O_B g_B)(g_A O_A)^{-1}, \tag{3.3}$$

where O_i is the i^{th} grain's material-specific symmetric operator. The feature first converts all grain Euler angles into quaternions to simplify calculations. To find all possible misorientation angles of two quaternions, each quaternion will be rotated by all possible symmetry matrices. The minimum of all possible angles from two rotated quaternions is defined as the GB misorientation. Since the β-SiC found in TRISO particles is a cubic crystal, it has 24 symmetric operators. Each GB misorientation will be calculated 24×24 ways to make sure all the orientations are in the same fundamental zone and to obtain the minimal misorientation.

3.2.1.2 Verification for all possible GBs in a polycrystal

The implementation of the new feature is verified by comparing its predictions to the expected result from a 2D polycrystalline structure with 10 grains. The reference grain has an orientation of 0° around the out-of-plane axis, and the other grains are oriented with the specific θ values provided in Table 3.1. Table 3.1 also provides the expected misorientation angles, as well as the code's predictions for the misorientation of each grain with the reference grain. Note that the expected misorientation values are determined by leveraging the cubic crystal symmetry. For example, the misorientation between the reference grain ($\theta = 0°$) and the grain with $\theta = -60°$ is 30°. The new feature accurately predicts the GB misorientations in polycrystals.

θ (°)	Expected (°)	Calculated (°)
0	0	0.0
30	30	30.0
44	44	44.0
45	45	45.0
46	44	44.0
60	30	30.0
90	0	0.0
-30	30	30.0
-60	30	30.0

Table 3.1. Verification results: expected and calculated misorientation angles for different grains with an orientation equal to θ. The new feature provides an accurate method to calculate the GB misorientation in polycrystals.

3.2.1.3 GB types determination by misorientation angle

Once the GB misorientation angle has been computed, the GB type t_{GB} is defined as

$$t_{GB} = 2 - \frac{\sum_{LAGB}(\eta_i^2\eta_j^2)}{\sum_{GB}(\eta_i^2\eta_j^2)}, \tag{3.4}$$

where η_i and η_j are the order parameters for two neighboring grains i and j. The order parameter is defined as 1 in some grains and as 0 in neighboring grains and continuously transitions from 1 to 0 at the GB. The denominator in the equation sums the $\eta_i^2\eta_j^2$ for all grain combinations. The numerator sums the $\eta_i^2\eta_j^2$ for the grain combinations for LAGB only (i.e., misorientation angle $< 15°$). Therefore, t_{GB} is equal to 0 within the grains, 1 at LAGBs, 2 at HAGBs, and an interpolated value between 1 and 2 for the triple junction between two GB types. In Fig. 3.5(b), the GB type is determined on a 2D 1000 $nm \times$ 1000 nm polycrystal with 50 grains (Fig. 3.5(a)) to illustrate the process.

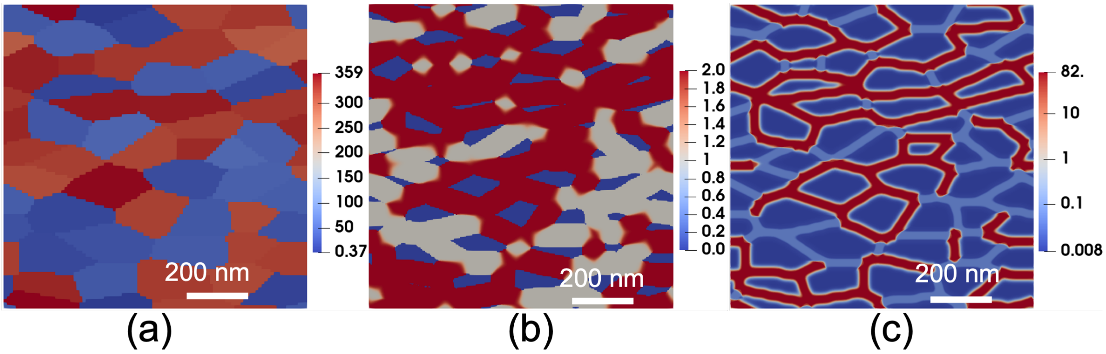

Figure 3.5. Illustration of new feature to determine GB types. (a) shows grain orientation, (b) shows the GB type: 0 within the grains, 1 at LAGBs, and 2 at HAGBs, and (c) shows the assigned local diffusivity with log-scale color map continuously across the polycrystal.

3.2.1.4 Local diffusivity assignment for the bulk, LAGBS, and HAGBs

After obtaining the GB types from the grain orientations, MOOSE computes the parameter χ to describe the location of GBs. The GB parameter χ is defined as

$$\chi = \sum_i^N \eta_i^2, \tag{3.5}$$

where N is the number of order parameter. χ is equal to 1 in the grain interior, while continuously transitioning to 0.5 along the middle of GB. To distinguish the LAGB and HAGB, a new χ_{GBj} is defined as

$$\chi_{GBj} = s_j + (1 - s_j)\sum_i^N \eta_i^2, \tag{3.6}$$

where χ_{GBj} is regarded as χ_{LAGB} or χ_{HAGB} for corresponding GB types with different s_j. s_j is defined as

$$s_j = |t_{specific,j} - t_{imported}|, \tag{3.7}$$

where $t_{imported}$ is the GB type field defined in Eq. (3.4), and $t_{specific,j}$ is the specific GB type set by a user to calculate the χ_j parameter. For example, the resulting field in Fig. 3.5 (b) is the $t_{imported}$ for the polycrystal in Fig. 3.5 (a). It is equal to 0 in the bulk, 1 in LAGBs, and 2 in HAGBs. To define χ_{LAGB}, $t_{specific,LAGB}$ is set to 1, and s_{LAGB} would therefore be equal to 0 in LAGBs and equal to 1 elsewhere. As a result, χ_{LAGB} is equal to 1 in the grains' interiors and HAGBs, while continuously transitioning to 0.5 in the middle of LAGBs. Similarly, to define χ_{HAGB}, $t_{specific,HAGB}$ is set to 2 so that s_{HAGB} equals to 0 in HAGBs and equals to 1 elsewhere. As a result, χ_{HAGB} is equal to 1 in the grains' interiors and LAGBs, while continuously transitioning to 0.5 in the middle of HAGBs. Based on the two continuous descriptions for two GB types, the local diffusivity D is defined as

$$D = (1 - h_{GB}(\chi))D_b + h_{GB}(\chi)\frac{h_{GB}(\chi_{LAGB})}{h_{GB}(\chi_{LAGB}) + h_{GB}(\chi_{HAGB})}D_{LAGB} + \frac{h_{GB}(\chi_{HAGB})}{h_{GB}(\chi_{LAGB}) + h_{GB}(\chi_{HAGB})}D_{HAGB}, \tag{3.8}$$

where D_b, D_{LAGB}, and D_{HAGB} are the diffusivities for bulk, LAGB, and HAGB, and h_{GB} is the interpolation function at the GBs. h_{GB} is defined in Ref. [3] as

$$h_{GB}(\chi) = 1 - \frac{1}{2}\left(1 + tanh\left((\chi - \chi_0)\frac{2tanh^{-1}(0.8)}{\Delta}\right)\right), \tag{3.9}$$

where χ can be either as defined in Eq. (3.5) to represent all the GBs or as defined in Eq. (3.6) to represent the LAGBs or the HAGBs. $h_{GB}(\chi)$ describes the interpolation function for all GBs, $h_{GB}(\chi_{LAGB})$ describes the interpolation function for LAGBs, and $h_{GB}(\chi_{HAGB})$ describes the interpolation function for HAGBs. $\chi_0 = 0.75$ is used to make $h(\chi_0) = 0.5$, and Δ is the distance $|\chi_{0.9} - \chi_{0.1}|$ for $h_{GB}(\chi_{0.1}) = 0.1$ and $h_{GB}(\chi_{0.9}) = 0.9$. $h_{GB}(\chi)$ aims to be equal to 0 where $\chi = 0$ and equal to 1 when $\chi = 0.5$. When $\Delta = 0.11$, $|h_{GB}(0.5) - 1|$ and $|h_{GB}(1) - 0|$ are smaller than 10^{-4} [3]. The small difference makes $h_{GB}(\chi)$ approach 1 in GB areas and approach 0 in bulk areas. As Fig. 3.5(c) shows, the local diffusivity will be assigned different values based on different GB types, continuously transitioning at triple junctions.

3.2.1.5 Scaling the diffusivity in bulk, LAGB, and HAGB

The bulk, LAGB, and HAGB Ag diffusivities in SiC derived from lower length scale simulations are then used with the newly developed feature described above to compute the effective Ag diffusivity in polycrystalline SiC [2, 3]. However, as described in Ref. [3], to limit computational costs, simulations require using a non-physical GB width that can be several times larger than realistic GB width. This approach has already been developed and tested in Ref. [3] for two different diffusivities (i.e., bulk and GB diffusivities). However, it must now be expanded to three different diffusivities: bulk, LAGB, and HAGB. In this work, we update this approach to appropriately scale up three diffusivities using the three microstructures shown in Fig. 3.6. The reference effective diffusivities D^{eff} defined using the microstructures are equal to

$$D^{eff}_{1,x} = \left(1 - \frac{w_{GB1} + w_{GB2}}{L}\right)D_b + \frac{w_{GB1}}{L}D_{GB1} + \frac{w_{GB2}}{L}D_{GB2}, \tag{3.10}$$

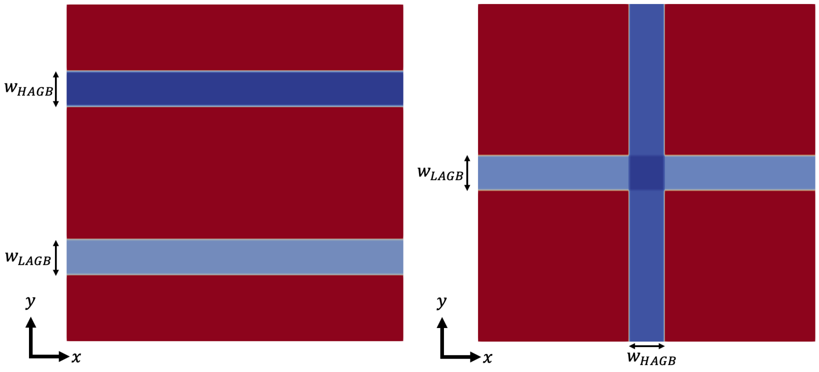

(a) (b)

Figure 3.6. Artificial microstructures used to develop a scale up approach for three diffusivities: bulk, LAGB, and HAGB. (a) shows the two parallel GBs, and (b) shows the two perpendicular GBs. In both cases, one GB is a LAGB, while the other is a HAGB.

$$D_{1,y}^{eff} = \frac{D_b D_{GB1} D_{GB2}}{\left(1 - \frac{w_{GB1}+w_{GB2}}{L}\right) D_{GB1} D_{GB2} + \frac{w_{GB1}}{L} D_{GB2} D_b + \frac{w_{GB2}}{L} D_{GB1} D_b}, \tag{3.11}$$

and

$$D_{2,x}^{eff} = \left(1 - \frac{w_{GB1}}{L}\right) \frac{D_b D_{GB2}}{\left(1 - \frac{w_{GB2}}{L}\right) D_{GB2} + \frac{w_{GB2}}{L} D_b} + \frac{w_{GB1}}{L} \frac{D_{GB1}(D_{GB1} + D_{GB2})/2}{\left(1 - \frac{w_{GB2}}{L}\right)(D_{GB1} + D_{GB2})/2 + \frac{w_{GB2}}{L} D_{GB1}}, \tag{3.12}$$

where GBi describes either a LAGB (i=1) or a HAGB (i=2), w_{GB_i} is the width of the corresponding GB, D_{GB_i} is the Ag diffusivity of the corresponding GB, D_b is the bulk diffusivity, and L is the length of the domain. As in Ref. [3], the reference values for D_b, D_{LAGB}, D_{HAGB}, w_{LAGB}, and w_{HAGB} are provided by lower length scale simulations and/or experimental measurements and define the values of $D_{1,x}^{eff}$, $D_{1,y}^{eff}$, and $D_{2,x}^{eff}$. Then, for given values of w_{LAGB} and w_{HAGB}, the system can be solved for the scaled-up values of D_b, D_{LAGB}, and D_{HAGB}. These diffusivity values can then be used to compute the effective Ag diffusivity in SiC without extensive errors due to using a larger than physical GB width.

3.2.1.6 Verification on grain structure with three parallel grains

To verify the new feature in MOOSE, we run the diffusion simulation in a 2D grain structure with three parallel grains. The structure domain is 100 *nm* × 100 *nm*, and all GB widths are 6 *nm*. As Fig. 3.7(a) shows, one upper GB is a LAGB, and the others are HAGBs. The local diffusivity over the dashed line in Fig. 3.7(a) is shown in Fig. 3.7(b). The diffusivity varies continuously across the grain structure and reaches the expected diffusivities in the bulk and the two GB types. There is an error in the bulk area because of the minimal value of interpolation function (see Section 3.2.1.4). However, the error is minor considering the low influence of bulk diffusivity on the effective diffusivity.

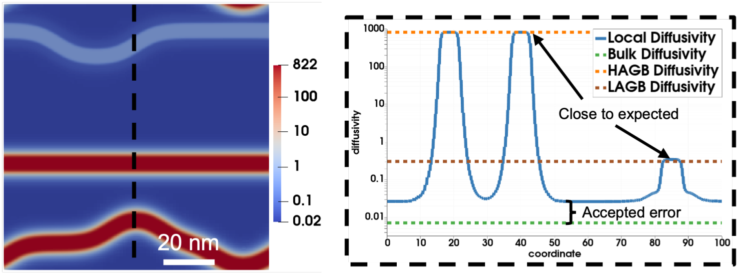

(a) (b)

Figure 3.7. The verification for the new feature in the three parallel grains structure with 100 *nm* × 100 *nm* domain and 6 *nm* GB size. (a) shows the assigned local diffusivity with a log-scale color map. (b) shows the local diffusivity plotted over the dashed line in (a).

3.2.1.7 Verification on grain structure with triple junctions

The new feature is verified on a grain structure with triple junctions to make sure the simulation can get accurate result on triple junctions. As Fig. 3.8(a) shows, there are five grains and eight triple junctions with 6 *nm* GB width in a 100 *nm* × 100 *nm* domain. Four triple junctions include grain combinations with LAGB and HAGB. The local diffusivity over the two crossing dashed lines in Fig. 3.8(a) are plotted on Fig. 3.8(b) and Fig. 3.8(c). The local diffusivity varies continuously across the triple junction and reaches the expected values in the bulk and the two GB types. As in Section 3.2.1.6, the error in the bulk area is accepted considering its minimal impact on the effective diffusivity.

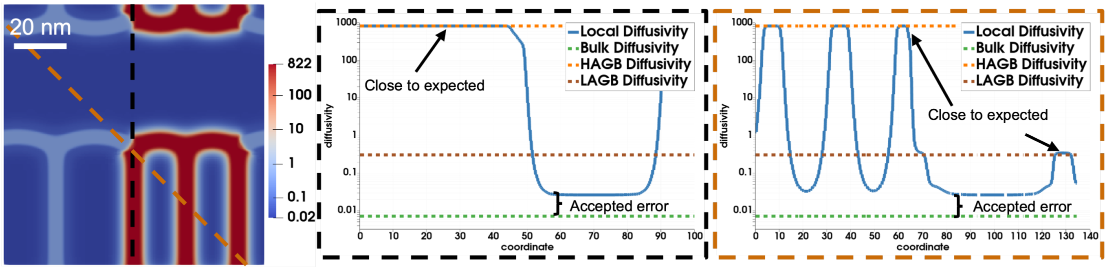

(a) (b) (c)

Figure 3.8. Verification of the new feature in a grain structure with five grains and a 6 *nm* GB size in a 100 *nm*×100 *nm* domain. (a) shows the assigned local diffusivity. (b) and (c) are the local diffusivities plotted over the two crossing dashed lines in (a). The outline colors of (b) and (c) are correspond to the color of the dashed lines in (a).

3.2.1.8 Influence of imported error in LAGB and bulk

Since the interpolation function h_{GB} is not exactly equal to 0 when $\chi = 0$, or to 1 when $\chi = 0.5$, some error is imported in the bulk, LAGB, and HAGB diffusivities. When HAGB diffusivity is more than 10^3 times larger than bulk diffusivity, the imported error is observable in Fig. 3.7(b) and Fig. 3.8(b). The error is acceptable because the bulk diffusivity only has minor influence on the effective diffusivity. However, the influence of the error will increase if the order of magnitude difference between HAGB diffusivity and bulk diffusivity increases. When HAGB diffusivity is more than 10^3 times larger than LAGB diffusivity, the imported error for the LAGB diffusivity also becomes noticeable. The large error will decrease the accuracy of effective diffusivity on diffusion model. It is therefore important to quantify the imported error and minimize it.

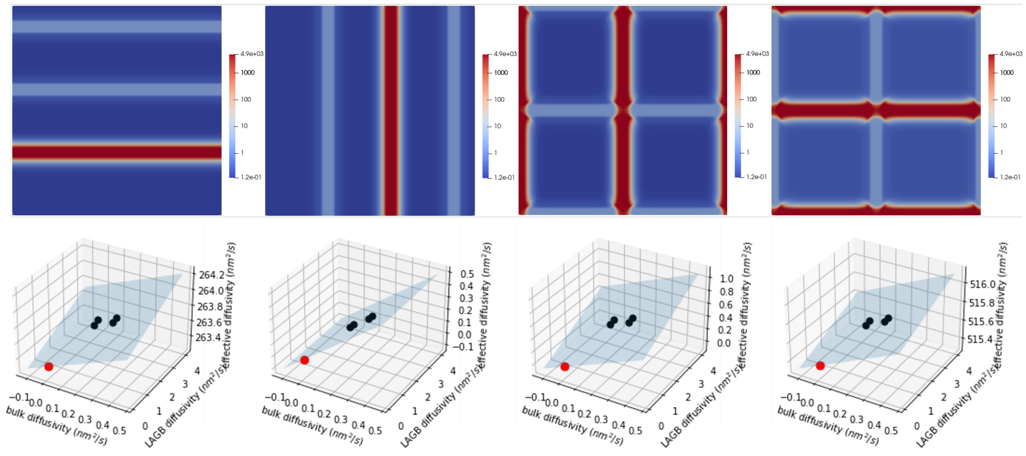

(a) (b) (c) (d)

Figure 3.9. Verification of the imported error in bulk and LAGB for four different grain structures with 6 *nm* GB width. (a) shows the three parallel grains with two LAGBs and one HAGB along the x-axis above, and below shows four simulations with different bulk and LAGB diffusivities (black points) and a derived corrected effective diffusivity (red point) fitting from the four simulations. (b) shows the three parallel grains with two LAGBs and one HAGB along the y axis above, and below shows four simulations with different bulk and LAGB diffusivities (black points) and a derived corrected effective diffusivity (red point) fitting from the four simulations. (c) shows the grain structure with three LAGBs along the x-axis and three HAGBs along the y axis above, and below shows four simulations with different bulk and LAGB diffusivities (black points) and a derived corrected effective diffusivity (red point). (d) shows the grain structure with three HAGBs along the x-axis and three LAGBs along the y axis above, and below shows four simulations with different bulk and LAGB diffusivities (black points) and a derived corrected effective diffusivity (red point). The domain size is $100\ nm \times 100\ nm$.

As Fig. 3.9 shows, the diffusion model was run on four different grain structures to get the effective diffusivity along the x-axis. The bulk, LAGB, and HAGB diffusivities provided by atomistic calculations are 7.01×10^{-21}, 1.74×10^{-18}, and $4.93\times10^{-15}\ m^2/s$, respectively [2, 35]. On each grain structure, the corrected effective diffusivity with expected bulk and LAGB diffusivities is extrapolated from the linear fit performed on the four simulations with minor differences on bulk and LAGB diffusivities. The comparison between the exact effective diffusivity and effective diffusivity with imported error shows that the errors of effective diffusivity for the four structures are 0.045%, 423.236%, 50.998%, and 0.021%, respectively. From these results, the imported error in bulk and LAGB diffusivities only has minor influence for the grain structures in Fig. 3.9 (a) and (d). The major reason is that the diffusion in these two structures is dominated by the HAGB, so the error in bulk diffusivity for the effective diffusivity is negligible. However, the imported error has a large influence for the grain structure in Fig. 3.9 (b) and (c) because the diffusion in these two structures is dominated by bulk and LAGB instead of HAGB.

One method to avoid the extra error on effective diffusivity is to optimize the interpolation function h_{GB}. If the $|h_{GB}(0.5) - 1|$ and $|h_{GB}(1) - 0|$ are smaller than 10^{-8}, the imported error for bulk and LAGB diffusivities will be 0.7% and 0.003%, respectively, and the error for effective diffusivity will be minor in all microstructures. The parameters χ_0 and Δ in optimized interpolation function are 0.75 and 0.0596 and should replace the parameter values defined under Eq. (3.9) to limit imported errors. The verification for the same three parallel grains structure with the optimized interpolation function parameters is shown in Fig. 3.10. The scaling method is applied for the diffusivity data from DFT to appropriately define the bulk and GB diffusivities when scaling up the GB width. In Fig. 3.10 (b), the local diffusivity reaches the expected value in bulk, LAGB, and HAGB without obvious error. Therefore, the optimized interpolation function parameters are helpful to decrease the error in effective diffusivity calculations.

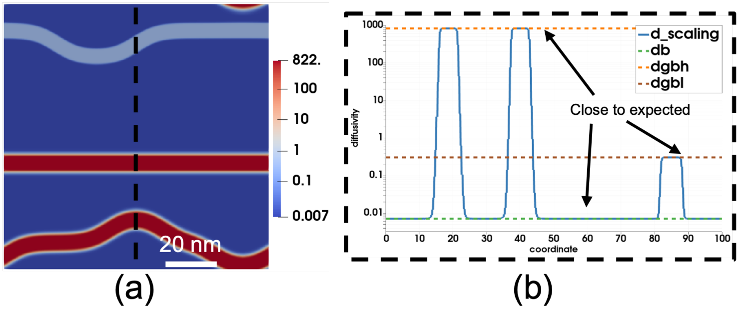

Figure 3.10. The verification for the optimized interpolation function parameters in three parallel grains structure in a 100 *nm* × 100 *nm* domain with a GB width of 6 *nm*. (a) shows the assigned local diffusivity with a log-scale color map. (b) shows the local diffusivity plotted over the dashed line in (a), which shows no noticeable error.

3.3 Summary and Expected Effects of SiC Texture on Ag Diffusivity at the Mesoscale

In this section, we presented MD simulations of Ag diffusivity in different SiC GB types and showed that the GB types can have a significant effect on Ag diffusion in SiC GBs. One of the main takeaways is that LAGB ($\Sigma 5$ (210)/[001]) Ag diffusivity is predicted to be faster than HAGB Ag diffusivity. We then presented a new feature that was developed in MOOSE to be able to read EBSD data and identify the GB type of each GB based on the grain orientation and attribute the desired diffusivity to each GB type. This feature was verified and merged into MOOSE. Furthermore, the approach developed in Refs. [2, 3] to scale up the GB size to decrease computational cost without introducing error in diffusivity values has been extended to three different diffusivity values. This limits errors when scaling up a microstructure with bulk, LAGB, and HAGB diffusivities.

In future work, simulations with different microstructures will be used to study the influence of microstructure on Ag release. The detailed microstructure parameters are grain size, aspect ratio, and HAGB percentage. In Fig. 3.11, the local diffusivity figures illustrate how we can study the influence of microstructure by altering one microstructure parameter at a time. The polycrystal in Fig. 3.11 (a) has large size grains, a large HAGB percentage, and a grain aspect ratio of 1. The polycrystal in Fig. 3.11 (b) uses a smaller HAGB percentage than in Fig. 3.11 (a). The polycrystal in Fig. 3.11(c) uses a smaller grain size than in Fig. 3.11(a). The polycrystal in Fig. 3.11(d) uses a grain aspect ratio of 3 Fig. 3.11(a).

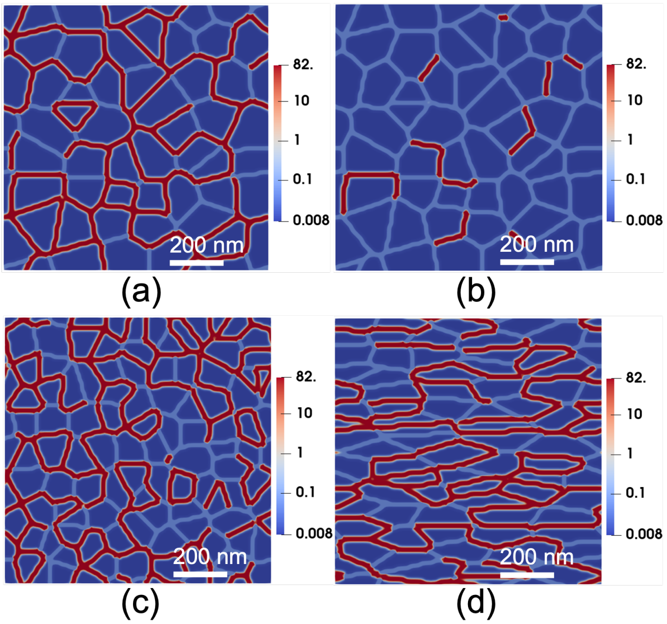

(a) (b) (c) (d)

Figure 3.11. The local diffusivity for different grain microstructures on polycrystalline in 1000 *nm* × 1000 *nm* domain. (a) shows a polycrystal with large size grains, a large HAGB percentage, and a grain aspect ratio of 1. The aspect ratio is the proportional relationship between a grain's width and height. (b) shows a polycrystal with large size grains, a small HAGB percentage, and a grain aspect ratio of 1. (c) shows a polycrystal with small size grains, a large HAGB percentage, and a grain aspect ratio of 1. (d) shows a polycrystal with large size grains, a large HAGB percentage, and a grain aspect ratio equal to 3. Since we expected HAGBs to diffuse faster than LAGBs, this figure shows higher diffusivities in HAGBs than in LAGBs. This will be corrected in future work to account for the results from Section 3.1.

Eventually, the new developments presented in Chapters 2 and 3 will be combined into one comprehensive model including temperature, microstructure, GB types, and irradiation effects. Since Ag diffusivity has been found to be higher in $\Sigma 5$ (210)/[001] GBs than in HAGBs, and because irradiation enhance diffusivity, we expect the future mesoscale effective Ag diffusivity to be closer to empirical values, therefore reducing the need for a correction factor [2, 3] to accurately predict Ag release from TRISO particles. Moreover, as was done in Ref. [3], the new model with will be validated against Ag release measurements from the first and second irradiation campaign in Advanced Gas-cooled Reactors (AGR-1 and AGR-2).

4. PALLADIUM PENETRATION MODEL

In FY-22, AIMD simulations have been performed to study the interfacial reaction between Pd metal and SiC at 2000 K. As shown in Figure 4.1, Pd atoms will chemically attack the SiC surface and lead to its disintegration. It can be seen that C atoms are removed from SiC lattice and form chain-like structures. In contrast to Pd, AIMD simulations show that Ag atoms are repelled from the SiC surface instead of reacting with it (see Figure 4.2). These results suggest that Pd attack of the SiC surface is an important first step in the diffusion of Ag through the SiC layer. A more detailed study of the Pd penetration model will be carried out in FY-23.

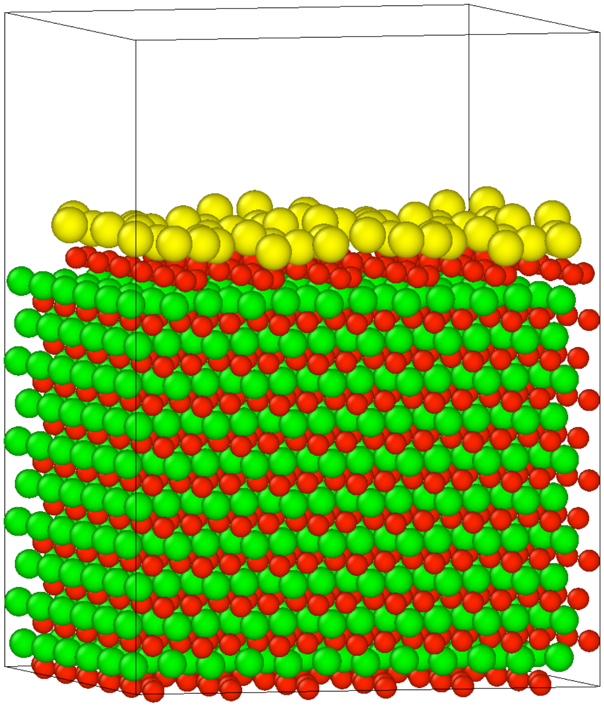

(a) t=0 ps

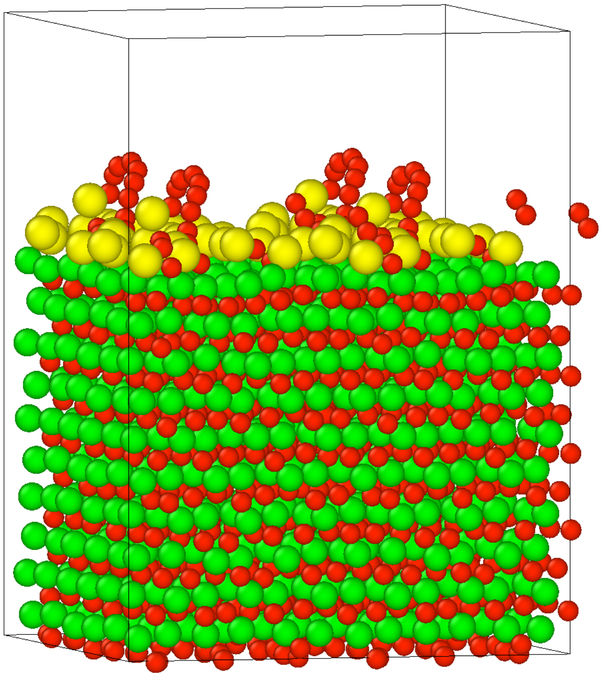

(b) t=7 ps

Figure 4.1. Snapshots of AIMD simulations of Pd interaction with SiC at 2000 K. The green, red, and yellow spheres represent Si, C, and Pd atoms, respectively.

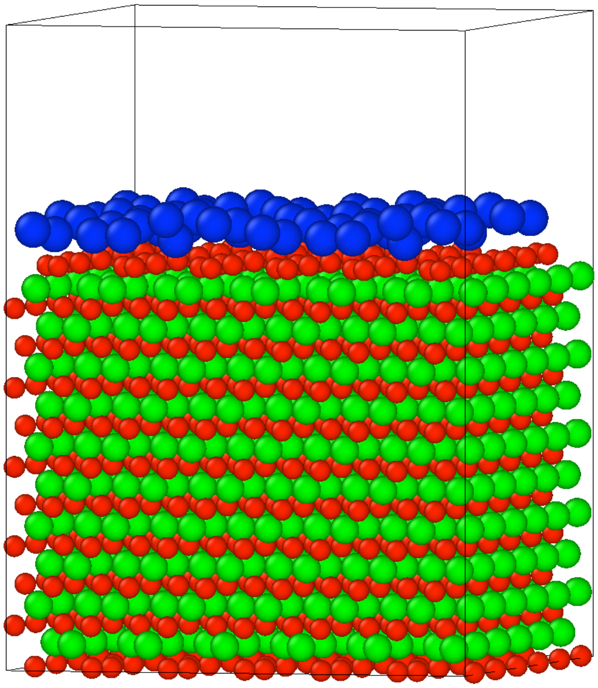

(a) t=0 ps

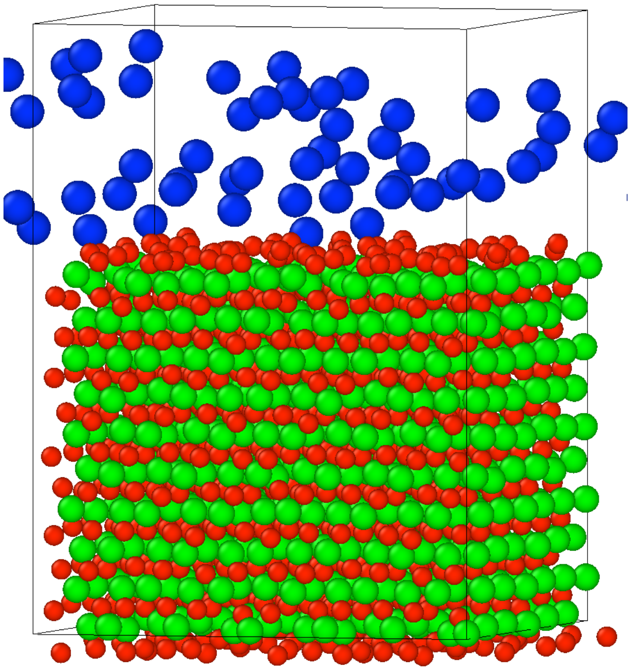

(b) t=7 ps

Figure 4.2. Snapshots of AIMD simulations of Ag interaction with SiC at 2000 K. The green, red, and blue spheres represent Si, C, and Ag atoms, respectively.

5. CONCLUSION

In Chapter 2, rate theory modeling of radiation-enhanced Ag diffusion in bulk SiC was performed. The results show that under the AGR-1 condition, the transition from thermal diffusion to radiation-enhanced diffusion of carbon vacancies can happen at a temperature between 1500 and 2100 K, and the radiation effect is more pronounced as temperature decreases. The predicted radiation-enhanced Ag diffusivity in the bulk is still orders of magnitude slower than that reported by experimental studies, which indicates that GB diffusion is the more dominant mechanism for Ag transport. The newly derived diffusivity of Ag in the bulk SiC is used to inform the engineering scale modeling and simulations.

In Chapter 3, we presented MD simulations of Ag diffusivity in different SiC GB types and showed that the GB types can have a significant effect on Ag diffusion in SiC GBs. Remarkably, LAGB ($\Sigma5$ (210)/[001]) Ag diffusivity is predicted to be faster than HAGB Ag diffusivity. To include different GB diffusivities in the multiscale approach to derive Ag effective diffusivity, a new feature has been developed, verified, and merged into MOOSE. It reads EBSD data and identifies the GB type of each GB based on the grain orientation. Then, it attributes the desired diffusivity to each GB type, therefore accounting for bulk, HAGB, and LAGB diffusivities.

Eventually, the new developments presented in Chapters 2 and 3 will be combined into one comprehensive model of effective Ag diffusivity including temperature, microstructure, GB types, and irradiation effects. Since Ag diffusivity has been found to be higher in $\Sigma5$ (210)/[001] GBs than in HAGBs, and because irradiation enhances diffusivity, we expect the future mesoscale effective Ag diffusivity to be closer to empirical values, therefore reducing the need for a correction factor [2, 3] to accurately predict Ag release from TRISO particles. Moreover, as was done in Ref. [3], the new model will be validated against Ag release measurements from the first and second irradiation campaign in Advanced Gas-cooled Reactors (AGR-1 and AGR-2).

Bibliography

[1] Jason D. Hales et al. “Modeling fission product diffusion in TRISO fuel particles with Bison”. In: *Journal of Nuclear Materials* 548 (2021), p. 152840.

[2] C. Jiang et al. *Atomistic and mesoscale simulations to determine effective diffusion coefficient of fission products in SiC*. Idaho National Laboratory, 2021.

[3] Pierre-Clément A. Simon et al. “Mechanistic calculation of the effective silver diffusion coefficient in polycrystalline silicon carbide: Application to silver release in AGR-1 TRISO particles”. In: *Journal of Nuclear Materials* 563 (May 2022), p. 153669. ISSN: 0022-3115. DOI: `10.1016/J.JNUCMAT.2022.153669`.

[4] R Devanathan, WJ Weber, and F Gao. “Atomic scale simulation of defect production in irradiated 3C-SiC”. In: *Journal of Applied Physics* 90.5 (2001), pp. 2303–2309.

[5] Jia-Hong Ke and Benjamin W. Spencer. “Cluster dynamics modeling of Mn-Ni-Si precipitates coupled with radiation-induced segregation in low-Cu reactor pressure vessel steels”. In: *Journal of Nuclear Materials* 569 (2022), p. 153910.

[6] Jia-Hong Ke et al. “Cluster dynamics modeling of Mn-Ni-Si precipitates in ferritic-martensitic steel under irradiation”. In: *Journal of Nuclear Materials* 498 (2018), pp. 83–88.

[7] Jia-Hong Ke et al. “Flux effects in precipitation under irradiation – Simulation of Fe-Cr alloys”. In: *Acta Materialia* 164 (2019), pp. 586–601.

[8] Benjamin J Cowen et al. “Investigations of irradiation effects in crystalline and amorphous SiC”. In: *Journal of Applied Physics* 126.13 (2019), p. 135902.

[9] Ming-Jie Zheng et al. “Energy barriers for point-defect reactions in 3*C*-SiC”. In: *Phys. Rev. B* 88 (5 2013), p. 054105.

[10] T. R. Waite. “General Theory of Bimolecular Reaction Rates in Solids and Liquids”. In: *The Journal of Chemical Physics* 28.1 (1958), pp. 103–106. DOI: `10.1063/1.1744051`.

[11] G.R. Odette and Randy Nanstad. “Predictive reactor pressure vessel steel irradiation embrittlement models: Issues and opportunities”. In: *JOM* 61 (July 2009), pp. 17–23.

[12] N. Soneda. “11 - Embrittlement correlation methods to identify trends in embrittlement in reactor pressure vessels (RPVs)”. In: *Irradiation Embrittlement of Reactor Pressure Vessels (RPVs) in Nuclear Power Plants*. Ed. by Naoki Soneda. Woodhead Publishing Series in Energy. Woodhead Publishing, 2015, pp. 333–377.

[13] H.L. Heinisch et al. "Displacement damage in silicon carbide irradiated in fission reactors". In: *Journal of Nuclear Materials* 327.2 (2004), pp. 175–181.

[14] Blaise P. Collin. "AGR-1 Irradiation Test Final As-Run Report, Rev. 3". In: (Jan. 2015). DOI: `10.2172/1173081`.

[15] David Shrader et al. "Ag diffusion in cubic silicon carbide". In: *Journal of Nuclear Materials* 408.3 (2011), pp. 257–271. ISSN: 0022-3115.

[16] Hyunseok Ko et al. "Ag diffusion in SiC high-energy grain boundaries: Kinetic Monte Carlo study with first-principle calculations". In: *Computational Materials Science* 121 (2016), pp. 248–257. ISSN: 0927-0256. DOI: `https://doi.org/10.1016/j.commatsci.2016.04.027`. URL: `https://www.sciencedirect.com/science/article/pii/S0927025616301860`.

[17] J.J. van der Merwe. "Evaluation of silver transport through SiC during the German HTR fuel program". In: *Journal of Nuclear Materials* 395.1 (2009), pp. 99–111. ISSN: 0022-3115.

[18] Moormann R. Verfondern K. Martin R.C. *Methods and data for HTGR fuel performance and radionuclide release modeling during normal operation and accidents for safety analysis*. 1993.

[19] Winfried Amian and Detlev Stöver. "Diffusion of Silver and Cesium in Silicon-Carbide Coatings of Fuel Particles for High-Temperature Gas-Cooled Reactors". In: *Nuclear Technology* 61.3 (1983), pp. 475–486.

[20] H. Nabielek, P. E. Brown, and P. Offermann. "Silver Release from Coated Particle Fuel". In: *Nuclear Technology* 35.2 (1977), pp. 483–493.

[21] Hyunseok Ko, Izabela Szlufarska, and Dane Morgan. "Cs diffusion in SiC high-energy grain boundaries". In: *Journal of Applied Physics* 122.10 (2017), p. 105901.

[22] Pierre-Clément Simon et al. "Jupyter script for automatic polycrystalline generation with desired grain size and elongation." In: *Mendeley Data,* V1, doi: 10.17632/vh78xyy85f.1 (2021). DOI: `10.17632/VH78XYY85F.1`.

[23] Cody J. Permann et al. "Order parameter re-mapping algorithm for 3D phase field model of grain growth using FEM". In: *Computational Materials Science* 115 (Apr. 2016), pp. 18–25. ISSN: 0927-0256. DOI: `10.1016/J.COMMATSCI.2015.12.042`.

[24] J. D. Hales et al. "Asymptotic expansion homogenization for multiscale nuclear fuel analysis". In: *Computational Materials Science* 99 (Mar. 2015), pp. 290–297. ISSN: 09270256. DOI: `10.1016/j.commatsci.2014.12.039`.

[25] Michael R. Tonks et al. "An object-oriented finite element framework for multiphysics phase field simulations". In: *Computational Materials Science* 51 (1 Jan. 2012), pp. 20–29. ISSN: 09270256. DOI: `10.1016/j.commatsci.2011.07.028`.

[26] Cody J. Permann et al. "MOOSE: Enabling massively parallel multiphysics simulation". In: *SoftwareX* 11 (2020). ISSN: 23527110. DOI: `10.1016/j.softx.2020.100430`. arXiv: `1911.04488`. URL: `http://arxiv.org/abs/1911.04488`.

[27] Derek Gaston et al. "MOOSE: A parallel computational framework for coupled systems of nonlinear equations". In: *Nuclear Engineering and Design* 239 (10 Oct. 2009), pp. 1768–1778. ISSN: 00295493. DOI: `10.1016/j.nucengdes.2009.05.021`.

[28] Rainer Moormann and Karl Verfondern. *Methodik umfassender probabilistischer Sicherheitsanalysen für zukünftige HTR-Anlagenkonzepte Ein Statusbericht (Stand 1986) Band 3 : Spaltproduktfrelsetzung*. Tech. rep. Institut für Nukleare Sicherheitsforschung Jül-Spez-388. 0343-7639, 1987.

[29] *Fuel performance and fission product behaviour in gas cooled reactors (Technical Report) | ETDEWEB*. Tech. rep. IAEA. IAEA-TECDOC-978, Nov. 1997. URL: `https://www.osti.gov/etdeweb/biblio/616984`.

[30] Blaise P. Collin et al. "Comparison of silver, cesium, and strontium release predictions using PARFUME with results from the AGR-1 irradiation experiment". In: *Journal of Nuclear Materials* 466 (Nov. 2015), pp. 426–442. ISSN: 0022-3115. DOI: `10.1016/J.JNUCMAT.2015.08.033`.

[31] Tyler J. Gerczak et al. "SiC layer microstructure in AGR-1 and AGR-2 TRISO fuel particles and the influence of its variation on the effective diffusion of key fission products". In: *Journal of Nuclear Materials* 480 (Nov. 2016), pp. 257–270. ISSN: 0022-3115. DOI: `10.1016/J.JNUCMAT.2016.08.011`.

[32] Haoyuan Qi et al. "Near–atomic-scale observation of grain boundaries in a layer-stacked two-dimensional polymer". In: *Science Advances* 6 (33 Aug. 2020). ISSN: 23752548. DOI: `10.1126/SCIADV.ABB5976/SUPPL_FILE/ABB5976_SM.PDF`. URL: `https://www.science.org/doi/10.1126/sciadv.abb5976`.

[33] S. Plimpton. "Fast parallel algorithms for short-range molecular dynamics". In: *J. Comput. Phys.* 117 (1995), pp. 1–19.

[34] Cody J. Permann et al. "MOOSE: Enabling massively parallel multiphysics simulation". In: *SoftwareX* 11 (Jan. 2020), p. 100430. ISSN: 23527110. DOI: `10.1016/j.softx.2020.100430`.

[35] Jeremy Rabone and Eddie López-Honorato. "Density functional theory metadynamics of silver, caesium and palladium diffusion at β-SiC grain boundaries". In: *Journal of Nuclear Materials* 458 (Mar. 2015), pp. 56–63. ISSN: 0022-3115. DOI: `10.1016/J.JNUCMAT.2014.11.032`.